NASA Contractor Report 178298

Predictions of Unsteady Wing and Pylon Forces Caused by Propeller Installation

(NASA-CR-178298) PREDICTIONS OF WING AND N87-24966
PYLON FORCES CAUSED BY PROPELLER
INSTALLATION (Cambridge Acoustical
Associates) 82 p Avail: NTIS HC A05/MF Unclas
A01 CSCL 20A G3/71 0082607

Rudolph Martinez

CAMBRIDGE ACOUSTICAL ASSOCIATES, INC.
Cambridge, MA 02140

Contract NAS1-18020
May 1987

NASA
National Aeronautics and
Space Administration

Langley Research Center
Hampton, Virginia 23665-5225

TABLE OF CONTENTS

TABLE OF CONTENTS (Continued)

SUMMARY AND CONCLUSIONS

Calculations have been carried out to predict unsteady-aerodynamic sources of wing structureborne vibration for various modes of propeller installation.

Mounted either upstream of the wing or downstream of the pylon that supports it, a propeller at cruise must chop through a steady but nonuniform inflow field. For a pusher propeller the largest source of nonuniformity is the wake of the upstream planform; for a tractor propeller it is the much smoother, and therefore less severe, upstream interference of the wing at the propeller disk plane. Both types of inflow generate a net harmonic propeller thrust, collected at the hub and acting to drive the wing or pylon in roughly the flight direction through the engine connections.

In the case of a tractor propeller the significant mechanism for generation of harmonic forces is the unsteady-aerodynamic reaction of the wing to the unsteady downwash induced by the convected propeller wake.

Both configurations and mechanisms have been analyzed here for operating conditions and geometric parameters corresponding to the Hamilton Standard high-efficiency propeller. On theoretical grounds we conclude that the upstream wing effect will not result in a significant source of vibration. Our calculations in this part of the study required that we first model the interference wing flows of the Gulfstream-II aircraft at the proposed propeller location.

For a pusher propeller cutting through its pylon's wake we have predicted a 40-lb thrust at the fundamental (blade-passage) frequency. The model of wake momentum deficit for a nonlifting pylon was here based on available full-scale measurements for the wing of a typical airliner; it used the average of pairs of data points above and below the wing plane, with the wake properly scaled down and applied at downstream stations where the propeller disk will likely be. Whether or not the 40-lb number will result in an unacceptable noise level depends on wing/cabin transfer functions not fully available yet, either theoretically or experimentally, and on whether the force can be isolated effectively, for example, through properly designed engine mounts.

We did not analyze fuselage interference or boundary-layer effects; however, for both wing- and aft-mounted propellers those flows should be bounded in degree of nonuniformity by the wing interference and pylon wake, with corresponding harmonic loads which fall between those predicted here.

Our estimates of wing pressure distributions due to wake impingement also await structural/acoustic calculations for a final conclusion.

A few general recommendations strictly based on the aerodynamics problems examined can be made, however:

Nonuniform Propeller Inflow as a Mechanism of Thrust Generation

1. Having a large number of blades is a good idea, not just from the steady-performance viewpoint, which seeks lower individual blade tip speeds while keeping design thrust constant, but also for the purpose of lowering unsteady propeller thrust levels. For a given propeller RPM use of more blades yields a higher value of reduced frequency associated with the blade-passage fundamental, and so in lower levels of noncompact blade-sectional loadings contributing to total thrust.

2. An obvious suggestion is that the number of propeller blades be kept even in the pylon-mounted, once-per-revolution excitation mode. For this configuration odd blades would yield better coupling between odd harmonics of thrust and those of the inflow nonuniformity and therefore would be undesirable. By the same reasoning, if a pusher propeller is ever considered for general wing installation, it should contain an odd number of blades since the excitation would then occur twice per revolution rather than once.

Wing Excitation by Wake of a Tractor Propeller

1. Similar to Item 1 above, a large number of blades will yield higher reduced frequencies based on wing semichord and flight speed,and so, in lower levels of wing pressure distributions for this mechanism.

2. Increasing the radius of the propeller should result in some decrease in strength of blade-tip vortices driving the downstream wing, essentially because keeping total performance thrust constant would then imply a more gradual spanwise load distribution for individual blades and a lower near-tip value of steady blade-sectional lift.

ACKNOWLEDGMENTS

The author wishes to thank members of NASA's Langley and Lewis Research Centers who provided needed data and related information: Dr. William Mayes, Mr. Irvin Loeffler, and Ms. Patricia Block; and colleagues from private industry who helped in similar ways: Mr. Robert Nazarowski and Mr. W.E. Arndt of the Lockheed-Georgia Company, and Mr. D. May of Douglas Aircraft Co., Long Beach.

NOMENCLATURE

b	blade semichord (Chapt. II), wing semichord (Chapt. III); dimensional
c_o	sound speed; dimensional
c_w	wing chord; dimensional
E, E^*	Fresnel Integral and conjugate, Eqs. II.25,26
g	wing thickness distribution (g' nondimensional)
G	function defined by Eqs. II.30, 31
h	wing camber distribution (h' nondimensional)
h_o	instantaneous normal-to-wing vortex position; dimensional
$k_m(R)$	gust wavenumber at radius R; dimensional
k	$\omega b/U$, reduced frequency
k_x	$k\cos\Lambda$, normal-to-blade leading edge wavenumber, equal to k in part of Appendix A
k_{ac}	normalized acoustic wavenumber $\omega b/c_o$
K	Possio kernel
ℓ	arc length along blade midchord; dimensional
L_{max}	maximum sectional steady blade lift; dimensional
$M(R), M$	circumferential Mach number for blade section at R, in Chapter II; flight Mach number in Chapter III
M_f	flight Mach number in Chapter II
N	number of blades
$p_{mN}, \bar{p}_{mN}$	wing pressure distribution and spanwise transform; dimensional
r	two-dimensional range measured from blade leading edge, Appendix A; nondimensional
R	radial distance to blade section in question; dimensional

R^*	Radial distance defined in Figs. II.4,5; dimensional
R_t^*	blade-tip value of R^*
R_t, R_h, R_{eff}	Tip, hub, and effective-tip radii in Eq. II.28; dimensional
$\bar{R}$	R_t/b
s	local spanwise blade coordinate; nondimensional
t	time; dimensional
T	unsteady blade thrust, Chapter II; steady-performance propeller thrust, Chapter III
T_m	harmonic of blade thrust; dimensional
T^{tot}	propeller thrust; dimensional
T^{tot}_{mN}	harmonic of propeller thrust; dimensional
$\tilde{T}_{mN}$	harmonic of sectional blade thrust; dimensional
u	nonuniform propeller inflow (Chapter II), or tangential velocity for shed wake (Chapter III)
u_t^*, u_ℓ^*	normal-to-wing leading edge interference horizontal flows due to thickness and lift, respectively; dimensional
u_t, u_ℓ	normal-to-propeller disk components of u_t^*, u_ℓ^*; dimensional
u_m	m^{th} Fourier component of u; dimensional
U	ΩR in Chapter II, flight speed elsewhere; dimensional
U_f	flight speed in Chapter II; dimensional
w	propeller-induced downwash velocity; dimensional
$w_{mN}, \bar{w}_{mN}$	harmonic of w, dimensional; and its spanwise Fourier transform
w^i, w^s	downwash velocity due to induced and shed-wake flows; dimensional
x	normal-to-leading edge coordinate (Chapter II for blade, Chapter III for wing); nondimensional
x_a	chordwise position of maximum camber displacement; dimensional
x_b	blade-based coordinate, Fig. II.3; nondimensional
x_f	horizontal coordinate normal to wing leading edge, Fig. II.2; dimensional

x_{o_f}	x_f position of propeller hub
$y(R^*), y_t$	blade mean-sweep function and tip value, Figs. II.4,5; dimensional
y	spanwise wing coordinate, Chapter III; nondimensional
y_a	maximum camber displacement; dimensional
$\tilde{y}$	yb
Y	x_f+iZ_f; dimensional
z	normal-to-wing coordinate; Chapter III; nondimensional
z_f	normal-to-wing coordinate; Chapter II; dimensional
z_{o_f}	z_f value of propeller hub
α	wing angle of attack
β	$\sqrt{1-M^2(R)\cos^2\Lambda(R)}$, Chapter II; or $\sqrt{1-M^2}$ based on flight Mach number, Chapter III
β_f	$\sqrt{1-M_f^2\cos^2\Lambda_w}$ (Chapter II)
β_t	angle of blade twist plus pitch
γ	strength of wake vortex sheet; dimensional
Γ	vortex strength; dimensional
ζ	$\mu+k_x/\beta^2$ in Appendix A; nondimensional
θ	angular position in blade polar reference frame (Appendix A); or circumferential angle in propeller disk (Chapter II)
$\Lambda(R), \Lambda_w$	circumferential component of blade sweep, wing sweep
μ	wavenumber parameter, Eq. II.24; nondimensional equal to kM/β^2 in Chapter III
$\tilde{\mu}$	frequency parameter; Eq. III.23; nondimensional
ρ	background density; dimensional

τ	wing thickness ratio
$\Phi, \Phi^*, \tilde{\Phi}$	perturbation velocity potentials; dimensional
Φ_{mN}	harmonic of Φ
ψ	wavenumber parameter, Eq. II.23; nondimensional
Ω	propeller rotational speed [rad/sec]
ω	$m\Omega N$

I. INTRODUCTION

An important task of the present research effort is the prediction of some of the new wing or pylon forces likely to be introduced by the aerodynamics of high-speed propellers. Estimates similar to those reported here will serve as input to aircraft-specific models of structureborne vibration for the wing and fuselage until more accurate calculations become widely available. We consider two possible mechanisms for the generation of such airloads:

First, chopping through the wake of an upstream supporting pylon will cause unsteady blade thrusts on a pusher propeller. If not properly isolated somewhere within the volume of the nacelle, the total thrust force will drive said pylon harmonically in a direction approximately colinear with that of flight, thereby producing fuselage vibration and cabin noise. The same can be expected of a wing-mounted tractor propeller cutting through the steady upstream interference field of the wing. The present study examines both modes of propeller installation.

Secondly, under the assumption of zero external interference or cross flows, steady operation of a tractor propeller has an associated system of helical blade-tip vortices which appear frozen in the rotating frame of the propeller, but on the wing plane induce an unsteady downwash distribution that in turn gives rise to unsteady pressures and lift.

Hanson[1] has developed what is probably the most general linear-regime formulation for lifting and nonlifting unsteady propfan flows. Given sufficient computing resources and time one could apply his model to analyze rigorously both situations listed above (standard lifting-surface theory being a special case of his integral equation, which therefore could be used for the wing as well). As earlier stated, however, our objective here is the less ambitious one of temporarily front-ending our own fairly detailed structural models for wing and fuselage with rough estimates for the aerodynamic forces which might drive them. To this end, predictions of unsteady thrusts for blades passing through either a pylon's wake or the wing's upstream interference field are here based on the following simple model:

The nonuniform propeller inflow field is broken up into a set of circumferential gusts at a chosen number of radial stations between hub and tip. For each of these we compute the value of blade sectional lift (thrust) using the approximation of local aerodynamic reaction implicit in high-frequency strip theory.[2] The model assumes zero blade pitch and twist, and so really addresses only the circumferential component of the aerodynamic problem ; it becomes more and more naturally valid for the radially outward, highly loaded blade sections at lower pitch.

At every blade section we neglect coupling between steady-performance and unsteady loadings. However, Myers and Kerschen[3] have determined that the omitted interaction could lead to O(1) underestimates of airfoil radiated noise, so that their results rationally suggest that our predictions here could be low by 6 dB. On the other hand, since at each blade section we apply a Mach number based on only circumferential motion, the effective decrease in compressibility through neglect of the flight speed component should result in some overestimate of sectional thrusts, thus partially offsetting the above neglected effect. The model also starts out under the assumption of no interference among blades, but later demonstrates that this simplification is indeed largely justified for the parameters in question.

The basic unsteady-aerodynamic theory is that by Adamczyk[4] for a swept ,rigid flat-plate airfoil passing through a gust; we apply it at each blade section using the local value of blade sweep, chord, and circumferential wave- and Mach numbers. Tip effects are simulated in an ad hoc fashion by allowing for decay of load amplitudes near the blade tip while keeping phases at their two-dimensional strip-theory values. In the final step individually integrated blade thrusts combine to yield the total thrust harmonic acting along the propeller axis.

For the mechanism of wing excitation by the propeller wake, the model uses a system of straight potential vortices appearing on the wing's Trefftz plane as a set of points rotating about the propeller axis; the downwash induced is constant across the wing chord because the vortices are taken to be aligned with the freestream direction. The wing is again a flat plate of constant chord and infinite span. The unsteady-aerodynamic theory this time is Amiet's[5] generalization of that in Ref. 4 to include plunging motion, valid for high subsonic flight speeds and/or high propeller blade-passage frequencies (it should be pointed out that Amiet has developed his theory for chordwise downwash distributions other than constant, thus allowing for the possibility of modelling some of the effects of actual vortex tilting relative to the wing chord. This further generalization, however, is not pursued here).

Weir[6] has recently analyzed the low-speed case of this mechanism.

Because the application to structureborne sound analysis for this mechanism uses continuous wing plating to interface with the source, predictions will here be in the form of a pressure distribution over the wing surface instead of a single load or moment, or running lift.

In summary, Section II will be devoted to the prediction of the time-varying point thrust propellers could feel due to several sources of non-uniformity in inflow, while Section III analyzes unsteady distributed wing airloads induced by the steady vortex wake of a tractor propeller.

II. PREDICTIONS OF HARMONIC AXIAL FORCES FOR PUSHER AND TRACTOR PROPELLERS IN NONUNIFORM STEADY INFLOW

A. Introduction

There are two prototypical configurations being considered for the new propfan technology. In one the propeller is mounted in the conventional sense, ahead of the wing, with the nacelle growing out of the latter. This mode of installation is currently undergoing tests on a Gulfstream II aircraft.

In the other basic design each nacelle is held near the stern by an outboard pylon connected directly to the fuselage. This type of installation will replace the aft-mounted turbojets now on T-tail aircraft such as the DC-9. It uses pusher instead of tractor propellers, whose wake flows do not impinge directly on any part of the aircraft, which therefore should be free of that type of excitation. However, since each propeller must then cut through the wake field of the upstream pylon supporting it, new unsteady blade loads are generated and transmitted to the wing via the engine structure unless isolated effectively.

This harmonic propeller thrust force is also present, though to a much less expected degree, for a tractor propeller passing through the upstream interference field of the wing. In the following sections we develop an analytical/numerical model to predict its spectra for both types of installation.

A basic assumption in the development is that blade-blade unsteady interference is negligible. In Appendix A we use the blade loads so computed and verify that mutually induced flows and pressures are in fact an order of magnitude lower than corresponding quantities for the incident gust field.

B. Models for Incident Velocity Fields

1. Pylon Wake Affecting Pusher Propeller

The wake of a pylon will be modelled using available measurements for the wing of a typical large aircraft.[7] Fig. II.1 shows mean-wake data for the 32%-chord station downstream from a wing's trailing edge. We shall construct the wake of a nonlifting (symmetric) pylon by taking the average of velocity deficits above and below the wing plane, thereby generating a figure similar to II.1 but for

$$1 - \frac{[u(z^+)+u(z^-)]}{2U_f} \quad .$$

We shall also adjust the data to generate wake profiles at stations other than the 32%-c_w downstream point. The procedure will be to apply Schlitchting's[8] simple mixing-length model for the diffusion of the two-dimensional wake behind a cylindrical body. He calculates that the rates of widening for the far wake and of reduction for the maximum velocity deficit are respectively proportional to the square- and inverse square-root of distance downstream of the object. Thus we have that $u(x,z=0)/u(x=32\%c_w,z=0)$ can be obtained from $\sqrt{1.32c_w/x}$ and $b_w(x)/b_{w32\%-c_w}$ from $\sqrt{x/1.32c_w}$, where b_w here denotes the "wake width" and x the distance downstream measured from the leading edge. By referencing x to the leading edge we generate a wake profile still fairly sharp at, say, one full chord downstream of the trailing edge ($x=2c_w$). If we used instead the trailing edge or even the mid-chord point, a more diffuse profile would result. The sharper profile is chosen because it yields conservative estimates for the blade-passage and higher harmonics of total propeller thrust.

2. Upstream Interference by the Wing

In the case of a tractor propeller the upstream wing interference for lifting and non-lifting wing flows at cruise will be computed by applying potential theory to the actual airfoil section of interest. The model uses a wing of infinite span and thus ignores wing-tip and fuselage effects at the propeller location. Compressibility and wing sweep enter the calculation through the Prandtl-Glauert factor $\sqrt{1-M_f^2\cos^2\Lambda_w}$, $M_f\cos\Lambda_w$ being the component of flight Mach number normal to the wing's leading edge.

Fig. II.2 shows the idealized wing propeller system for the upstream influence calculation. All complicating structures have been removed for simplicity. The perturbation velocities u* in the direction normal to the wing's leading edge are readily found from classical potential theory, e.g., Ref. 8: to be, for thickness and lifting flows,

$$\frac{u_t^*}{U_f\cos\Lambda_w} = \frac{\tau}{\pi\beta_f}\int_0^{c_w} d\bar{x}\,\frac{(x_f-\bar{x})g'(\bar{x})}{(x_f-\bar{x})^2+Z_f^2} \tag{II.1}$$

$$\frac{u_\ell^*}{U_f\cos\Lambda_w} = \frac{1}{\pi\beta_f}\,\mathrm{Re}\left\{\sqrt{\frac{c_w-Y}{Y}}\int_0^{c_w}\frac{d\bar{x}}{Y-\bar{x}}\sqrt{\frac{\bar{x}}{c_w-\bar{x}}}\,[h'-\alpha]\right\} \tag{II.2}$$

where c_w is the wing chord, U_f the flight speed, Λ_w the wing sweep, and $Z_f=z_f\beta_f$, where $\beta_f=\sqrt{1-M_f^2\cos^2\Lambda_w}$, with $M_f=U_f/c_o$, the flight Mach number. In Eq. II.2 $Y=x_f+iZ_f$. The f subscripts on x_f, z_f, and Z_f denote field points; on M_f, β_f f denotes the flight speed of the aircraft. In Eq. II.1 τ is the airfoil's thickness ratio and g'(x) is the surface slope function from leading to trailing edge. We shall model our wing as a four-digit NACA airfoil, for which the thickness function g' is given, by[9]

$$\begin{aligned} g'(x) &= .7423\sqrt{\frac{c_w}{x}} - .6300 - 3.5160\left(\frac{x}{c_w}\right) \\ &\quad + 4.2645\left(\frac{x}{c_w}\right)^2 - 2.030\left(\frac{x}{c_w}\right)^3 \end{aligned} \tag{II.3}$$

For the above "real" airfoil Eq. II.1 is inapplicable if one's objectives are pressures (or u^*) in the vicinity of the leading edge, essentially because the round nose violates the small-disturbance assumption of the theory. This defect, however, is local and should not seriously affect the interference calculation of interest here. Loading solutions for an elliptic airfoil discussed by Van Dyke[10], for example, indicate that even though the small-disturbance solution fails at the leading edge, it nevertheless yields the correct interference several nose radii away.

In Eq. II.2 h' is the slope of the mean-camber line, for a four-digit airfoil given by

$$h'(x) = \begin{cases} \dfrac{2y_a(x_a-x)}{x_a^2} & 0 \leq x \leq x_a \\ \dfrac{-2y_a(x-x_a)}{(c_w-x_a)^2} & x_a \leq x \leq c_w \end{cases} \tag{II.4}$$

where x_a is position between leading and trailing edge where the camber displacement has its maximum* value of y_a. In Eq. II.2 α stands for angle of attack.

As we have said, Eqs. II.1 and II.2 give the perturbation velocities in a direction normal to the swept leading edge. Of interest here are corresponding quantities u_t, u_ℓ in the direction normal to the propeller plane; in terms of $u^*_{\ell,t}$ these are obtained from

$$u_t = u^*_t \cos\Lambda_w \tag{II.5}$$

$$u_\ell = u^*_\ell \cos\Lambda_w \tag{II.6}$$

Referring to Fig. II.2, we note that field points on the propeller disk x_f and z_f are given by

$$x_f = x_{o_f} + R\sin\Lambda_w\cos\theta \quad , \quad x_{o_f} < 0 \tag{II.7}$$

$$z_f = z_{o_f} + R\sin\theta \tag{II.8}$$

where the value of R ranges from R_h at the propeller hub to R_t at the propeller tip.

Substituting Eqs. II.7,8 with II.1,2 into Eqs. II.5,6 yields the total upstream interference field

---

*The percent chord values of y_a, x_a take up the first two digits of the 4-digit NACA designation, and the thickness ratio the last two digits. Thus a NACA 2410 airfoil has $y_a/c_w = .02$, $x_a/c_w = .04$, $\tau = .1$.

$$u(R,\theta) = u_t(R,\theta)+u_\ell(R,\theta) \tag{II.9}$$

normal to the propeller plane as experienced by the blade section at radial position R as it travels from $\theta=0$ to $\theta=2\pi$.

C. Unsteady-Aerodynamic Model for Propeller

1. General Coupling Between Velocity and Lift

The nonuniform inflow field at the propeller plane, whether caused by upstream interference or by the pylon's wake, is now expressed at every radial station as a superposition of circumferential gusts:

$$u(R,\theta) = \sum_{m=-\infty}^{\infty} u_m(R)e^{-im\theta} \tag{II.10}$$

$$u_m(R) = \int_0^{2\pi} \frac{d\theta}{2\pi}\, u(\theta)e^{im\theta} \tag{II.11}$$

On the rotating frame of the propeller the speed of travel for each of the above gusts is $U(R)=\Omega R, R_h \leq R \leq R_t$; Ω is blade rotational speed in radians/sec, and the phase factors in Eq. II.10 become $m(\theta_j-\Omega t)$ for the j^{th} propeller blade turning in the clockwise direction (θ is defined positive in the counter-clockwise direction). Interpreting angular displacements in terms of local arc length, we have that

$$m\theta = \frac{m}{R}\cdot R\theta = k_m(R)b[\cos\Lambda(R)x_b+\sin\Lambda(R)\cdot s] \tag{II.12}$$

where $k_m(R)=m/R$ becomes the gust wavenumber value at radius R, $\Lambda(R)$ is the local blade sweep angle, $x_b\cos\Lambda=0$ the blade-based origin of the locally rectilinear circumferential direction, and s is the local spanwise, or radial, coordinate. The situation for a typical radial station is portrayed in Fig.II.3.

If the blade sweep's "radius of curvature" is much greater than the acoustic wavelength everywhere between hub and tip it should be possible to analyze each radial blade position as a locally straight planform passing through a gust of wavelength $2\pi R/m$ convected at local Mach number $M(R)=\Omega R/c_o$ at local blade sweep $\Lambda(R)$. Fig. II.4 shows how the latter is geometrically defined and calculated. We shall consider a family of radial sweep distributions given by the relation

$$y(R^*) = y_t(R^*/R_t^*)^n \tag{II.13}$$

where

$$R = \sqrt{R^{*2} + [y(R^*)]^2}, \quad R_t^* = \sqrt{R_t^2 - y_t^2} \tag{II.14}$$

where as indicated in Fig. II.5 y_t is the in-plane position of the blade tip relative to that were the blade not swept; $y_t=0$ in the analytical model corresponds to unswept blades. From Eq. II.13 and Fig. II.5 we have that

$$\Lambda(R) = \Lambda(\sqrt{R^{*2}+y^2}) = \tan^{-1}[\frac{\partial y(R^*)}{\partial R^*}] - \tan^{-1}[y/R] \tag{II.15}$$

We temporarily postpone further discussion of details of the unsteady aerodynamic calculation and for now simply observe that its goal is to yield a value of modal thrust T_m for each of the N blades cutting through gust m. For the j^{th} blade then, the time history of unsteady loading would be given by

$$T(t) = \sum_{m=-\infty}^{\infty} T_m \, e^{-im(\theta_j - \Omega t)} \tag{II.16}$$

where T_m is proportional to u_m. Taking $\theta_j = 2\pi(j-1)/N$, $j=1,2...,N$ for N equally spaced blades, we obtain the total propeller thrust as

$$\overset{tot}{T}(t) = \sum_{j=1}^{N} T_j(t) \tag{II.17}$$

Substituting Eq. II.16, interchanging orders of summation, and noting that

$$\sum_{j=1}^{N} e^{-im2\pi(j-1)/N} = \begin{cases} 0 & \text{if } m \neq \text{multiple of } N \\ N & \text{if } m = \text{multiple of } N \end{cases} \tag{II.18}$$

we have that

$$\overset{tot}{T}(t) = \sum_{m=-\infty}^{\infty} T_{mN}^{tot} \, e^{imN\Omega t}, \quad T_{mN}^{tot} = NT_{mN} \tag{II.19}$$

where $N\Omega$ is the blade-passage frequency; T_{mN} is proportional to u_{mN}, obtained from Eq. II.11:

$$u_{mN}(R) = \int_0^{2\pi} \frac{d\theta}{2\pi}\, u(R,\theta)\, e^{imN\theta} \qquad \text{(II.20)}$$

Quantities NT_{mN} for m=1,2..., represent the propeller thrust harmonics of primary issue here. The corresponding gust wavenumbers of interest are $k_{mN}(R)=mN/R$, etc.

2. Calculation of Modal Blade Sectional Thrusts

The sectional thrust (lb/ft) at radial station R corresponding to gust wavenumber k_{mN} is given by (gust interaction- and sweep angles both equal Λ):

$$\tilde{T}_{mN}(R) = \frac{2\pi b\rho U\cos\Lambda u_{mN}}{\beta} \cdot \frac{e^{-ik_s s}}{\sqrt{k_{mN} b \cos\Lambda/\beta^2+\mu}} \cdot$$

$$\begin{cases} \dfrac{1-i}{\pi}\, \dfrac{E^*[2(\mu-\psi)]}{\sqrt{\mu-\psi}} + f(\mu,\psi) & \text{for } \mu>\psi \\[2ex] \dfrac{1-i}{\pi}\, \dfrac{E[2(\psi-\mu)]}{\sqrt{\psi-\mu}} + f(\mu,\psi) & \text{for } \mu<\psi \\[2ex] \sqrt{\dfrac{1}{\pi}}\left[2+ \dfrac{(i-1)}{\pi} + \dfrac{2}{\pi}\left(1+ \dfrac{i}{8\mu}\right)E^*(4\mu) - \dfrac{ie^{-i4\mu}}{\pi^{3/2}\sqrt{2\mu}}\right] & \text{for } \mu=\psi \end{cases} \qquad \text{(II.21)}$$

with

$$f(\mu,\psi) = \frac{i}{\pi^{3/2}}\, \frac{1}{\mu-\psi} \left[e^{-2i(\mu-\psi)} \left\{\sqrt{\frac{2\mu}{\mu+\psi}}\, E^*[2(\mu+\psi)] - \frac{(1-i)}{2}\right\} + \frac{1-i}{2} - E^*(4\mu)\right] \qquad \text{(II.22)*}$$

---

* The last two terms of Eq. II.22, $\frac{1-i}{2} - E^*(4\mu)$, appear misprinted in Ref. 5 as $\frac{1+i}{2} - E^*(4\mu)$.

and where

$$\psi = \frac{k_{mN} b M^2 \cos^3\Lambda}{\beta^2} \qquad (= k_x M^2 \cos^2\Lambda/\beta^2, k_x = k_{mN} b \cos\Lambda) \qquad \text{(II.23)}$$

$$\mu = \frac{k_{mN} b}{\beta^2} \sqrt{M^2 \cos^2\Lambda - \sin^2\Lambda} \qquad \text{(II.24)}$$

with $\Lambda=\Lambda(R)$ given by Eq. II.15; $b=b(R)$ is the radially varying blade semichord; again, $k_{mN}=mN/R$, $M=M(R)=U(R)/c_o=\Omega R/c_o$ and $\beta = \sqrt{1-M^2\cos^2\Lambda}$; ρ is background density. $E(a)$ denotes a Fresnel integral of argument a;

$$E(a) = \int_0^a \frac{dt\ e^{it}}{\sqrt{2\pi t}} \qquad (\rightarrow \frac{1+i}{2} \text{ as } a\rightarrow\infty) \qquad \text{(II.25)}$$

so that its conjugate E* is given by

$$E^*(a) = \int_0^a \frac{dt\ e^{-it}}{\sqrt{2\pi t}} \qquad (\rightarrow \frac{1-i}{2} \text{ as } a\rightarrow\infty) \qquad \text{(II.26)}$$

The exponential factor $e^{-ik_s s}$ in Eq.II. 21 keeps track of the relative phase of sectional loads for different positions along the blade radius. Referring to Fig. II. 3 for the straight blade in rectilinear flight, the quantity $s\ .\ \sin\Lambda$ denotes the flow direction projection of the spanwise distance between two blade points. The phase factor should therefore be $\{-ik_{mN}b.s.\sin\Lambda\}$ or $\exp\{-ik_s s\}$ with $k_s=k_{mN}b\sin\Lambda$. In the standard literature the spanwise coordinate s usually carries the symbol "y" so that $\exp\{-ik_s s\}$ is $\exp\{-i"k_y y"\}$, with $"k_y y" = k_{mN} b \sin\Lambda y$ in agreement with the above argument.

The $\exp\{-ik_s s\}$ factor will be simulated here by analogy to the rectilinear case. The arc length difference in the direction of the incoming circumferential gust between radial station R and that at the hub is $R\sin^{-1}y/R$, with y given by Eq. II.13. The phase factor therefore becomes

$$e^{-ik_s s} = e^{-imN\sin^{-1}y/R} \qquad \text{(II.27)}$$

The slight relative shift in center of pressure, or lift (1/4 chord for steady lift), due to the variation in circumferential Mach number and gust wavenumber from blade hub to tip will not be taken into account (cf. discussion in Ref. 4, p. 24).

Finally, we wish to modify the basic sectional thrust distribution to account for the $\sqrt{R_t-R}$ load dropoff as R approaches the tip. Thus we choose a value of $R=R_{eff}$ where the sectional thrust will achieve approximately its maximum value, say at

$$R_{eff} = R_h + 75\%(R_t-R_h) \tag{II.28}$$

and define the total blade thrust harmonic T_{mN} for use in Eqs. II.16,19 as follows:

$$T_{mN} = \int_{R_h}^{R_t} d\ell\ \tilde{T}_{mN}[\ell(R)]G(R) \tag{II.29}$$

where ℓ denotes length along the blade and

$$G(R) = \begin{cases} 1 & \text{for } R_h \leq R \leq R_{eff} \qquad \text{(II.30)} \\ (a_o+a_1R)\sqrt{R_t-R} & \text{for } R_{eff} \leq R \leq R_t \qquad \text{(II.31)} \end{cases}$$

with

$$a_o = -\frac{R_{eff}}{2(R_t-R_{eff})^{3/2}} + \frac{1}{\sqrt{R_t-R_{eff}}} \tag{II.32}$$

$$a_1 = \frac{1}{2(R_t-R_{eff})^{3/2}} \tag{II.33}$$

Constants a_o, a_1 are determined from the continuity requirements for the sectional load and its slope at R_{eff}.

D. Application of Model

1. Propeller/Aircraft Geometry

Figures II.6a,b show front views respectively of a Hamilton Standard propfan prototype and of one of its blades.* The indicated dimensions are approximate projections on the propeller plane of actual propeller chord widths, etc. Our calculations will be based on them. The blade sweep distribution from hub to tip uses the midchord curve shown in Fig. II.6b; in applying the model earlier described and depicted in Fig. II.4,5 we found a curve with the power n=3 adequate for the present case.

Fig. II.7 shows top and side views of the installation geometry for a Gulfstream-II aircraft, and dimensions drawn for our calculations. Unfortunately, we were unable to obtain similar schematics for a pylon-mounted propeller; our calculations for this case are here based on assumed propeller locations downstream in terms of pylon chords. We use the 32% c_w and 100% c_w wake positions as measured from the pylon's trailing edge.

2. Models of Incident Velocity Fields

(a) Wake Signatures for Wing or Pylon

Fig. II.8 shows the result of fitting a two sided Gaussian to the wake measurements shown in Fig. II.1 for a lifting aircraft wing, and modelled velocity deficits experienced by two radial points on the propeller in their circumferential trajectory. The figure applies to a propeller with axis lying on the plane of the wing, which extends in the spanwise sense on both sides of the propeller. Only the $\theta=\pi$ spike will be used for a nonlifting pylon, and then symmetrized about its maximum value. The signature felt by the blade section near the hub (R_h) is wider than that at $R_{eff} \doteq .8\ R_{tip}$ because the effective wake takes up then a greater fraction of the total trajectory.

As a further illustration, Fig. II.9 shows the situation for a pusher wing-mounted propeller with axis at a distance above the wing plane corresponding to that of the Gulfstream-II nacelle (although a pusher

---

* I. Loeffler, NASA Lewis Research Center, personal communication.

wing-mounted propeller is presently not a candidate concept, we examine it also for completeness).

(b) Upstream Interference for Wing

Fig. II.10 shows predicted interference wing flows for the circumferential trajectory of $R=R_{eff}=.79\ R_{tip}\cong 3.5$ ft. The top insert shows both the cross-section of the Gulfstream-II wing* in a plane parallel to the flight direction, and the equivalent 4-digit NACA airfoil section in a plane roughly perpendicular to the leading edge (note Fig. II.7); $y_a/c_w=.013$, $x_a/c_w=.19$, thickness ratio $\tau=10\%$. A value of 1.5° was taken for the angle of attack. Point $\theta=0$ is inboard and axially closest to the wing (middle sketch and Fig. II.2a). Nonlifting interference is always negative; it is maximum at $\theta=0$. Lifting interference is positive above the wing (because the lift is positive) and negative below; it vanishes identically at the two points where the $R=R_{eff}$ cuts the extended plane of the wing.

3. Frequency/Mach Number Regime of Validity

Fig. II.11 shows the sweep distribution of the midchord curve traced out in Fig. II.6b. The other curve is a plot of Eq. II.24. After comparing approximate results with other more rigorous calculations, Amiet (Ref. 5, p. 1078) has determined that Adamczyk's high-frequency theory for a leading-edge flat plate passing through a gust at zero angle of attack should be reasonably accurate for $\mu>\pi/4$. If trailing-edge effects are included (as we have done here), he states that the results apply beyond a much lower value of μ. As far as compressibility and frequency effects in the propeller plane are concerned, we conclude that the μ curve in Fig. II.11 confirms the need and relevance of the noncompact aerodynamic model being applied. The values shown correspond to the fundamental $N\Omega=226$ Hz ($m=1$, $N=8$).

4. Predicted Blade Loadings and Total Propeller Thrust

(a) Pusher Propellers

Figs. II-12a,b are for a pusher propeller on an inboard nonlifting pylon at 32% and 100% chords downstream of the trailing edge. The axis of the propeller coincides with the midplane of the pylon. Each figure shows two curves: the wake field's fundamental harmonic as a

---

* W.E. Arndt, R.W. Nazarowski, Lockheed Georgia Co., personal communication.

function of radial position, $u_{mN}(R) = u_N(R)$; and the corresponding sectional blade thrust as given by the integrand of Eq. II.29. The 32%-c_w downstream wake is only slightly richer in N^{th} Fourier component than the 100%-c_w wake, with the largest differences appearing at the hub station.

Figs. II.13, 14 show predicted harmonics of total thrust T_{mN}^{tot} (Eq. II.19) for the two cases of Fig. II.12a,b. The 32-dB level for the fundamental corresponds to a 40-lb force acting along the propeller axis. Major differences between 32%-c_w and 100%-c_w curves appear to be postponed to higher frequencies.

Figs. II.15a,b show results for the unpursued concept of a wing-mounted pusher propeller; they correspond to propellers with (a) axis on the wing plane and, (b) axis elevated 1.78 ft above the wing plane. The axial propeller location is 32%-chord downstream from the trailing edge. The roughly doubled values in Fig. II.15a relative to those in Fig. II.12a reflect mostly the more effective coupling that exists for the "two-per-rev" wing over the once-per-rev pylon, given that the number of propeller blades is even (8). Fig. II.15b for the raised propeller displays a fairly erratic behavior in fundamental harmonic of incident velocity field (and associated sectional thrust).

Figs. II.16 and 17 show corresponding predictions of total thrust harmonic content. The 38-dB value for the fundamental in the $z_{o_f}=0$ case corresponds to a 70-lb force. The reduced value for 226 Hz in Fig. II.17b can be attributed to the relatively poor coupling some radial stations have to the 8^{th} Fourier modal number (Fig. II.15b).

(b) Tractor Propeller on a Gulfstream-II Wing

Fig. II.18 shows the propeller airload response to the combined lifting and nonlifting flows of Fig. II.10. The extremely low values (-48 dB$\cong$4x10^{-3}lb) suggest that this mechanism will not be significant. The reductions in level have two causes: first, the maximum interference amplitudes are low relative to those for the wakes previously examined, say 2-3% vs 20-25%; this difference, however, would account for only 20 dB relative to the wake results. More significantly, of course, is that the propeller is sufficiently removed in the upstream direction that the interference signature is a very smooth function of θ at all radial stations. Since the response couples only to multiples of the fundamental Fourier counter, which is high due to the number of blades, it would appear that low levels are virtually guaranteed for this mechanism.

E. Predicted Benefit of a Large Number of Blades in Reducing Harmonic Propeller Thrust

Eqs. II.19 and 21 point out that the theoretical total unsteady propeller thrust is proportional to $\rho(\Omega R)w_{mN}(\overline{k_{mN}b})^{-1}$.N.Blade Area, where $\overline{k_{mN}b}=mN\Omega b_{eff}/(\Omega R_{eff})=mNb_{eff}/R_{eff}$, an effective or average reduced frequency. We have assumed that its value is sufficiently high to approximate Eq. II.21 by its high-frequency asymptote, i.e., with $E^*=(1-i)/2$, etc. If we now write $w_{mN}=\alpha_{mN}^{eff}\Omega R$, where α_{mN}^{eff} is an effective instantaneous angle of attack in the quasi-steady aerodynamic sense, it follows that the unsteady thrust harmonic for the propeller is proportional to $\rho(\Omega R)^2(\overline{k_{mN}b})^{-1}$.N.Blade Area.

Now, the corresponding quantity for the design steady thrust may be similarly written as $\rho[U_f^2+\Omega^2R^2]$.N.Blade Area.$\bar{c}_L$, where $\bar{c}_L$ is an effective or spatially-averaged lift coefficient for each blade. With $\Omega R/U_f=O(1)$, we therefore obtain that the ratio of harmonic propeller thrust to propeller design thrust is proportional to

$$\frac{T_{mN}^{tot}}{T_{design}^{tot}} \propto \frac{1}{(\overline{k_{mN}b})\,\bar{c}_L} \qquad (II.34a)$$

$$\propto \frac{1}{N} \qquad (II.34b)$$

a vanishing quantity for high N for a family of propeller designs which keeps performance thrust constant. Having a large number of blades therefore makes sense from the perspective of propeller unsteady aerodynamics.

III. PREDICTIONS OF WING AIRLOADS INDUCED BY A PROPELLER WAKE

A. Introduction

The model for the propeller wake will here be essentially the same we developed in Ref. 11. A system of rotating straight potential vortices, one for each blade, radially located at the propeller tip positions. The path, or position, of the vortices is assumed unaffected by the presence of the wing -- unlike in more sophisticated treatments by Hardin and Mason,[12] of a similar situation at low speed, and by Lindblad,[13] for high speed. Also, we take each vortex to be aligned with the freestream direction, so that induced velocities over the wing chord are constant.

Even for this simple representation the system will be seen to induce a fairly complicated unsteady downwash distribution as function of spanwise location. In Ref. 11 we circumvented the development of a theory that would couple wing sectional airloads due to such an inflow by arguing that at high speeds (M=.8) and reduced frequencies individual spanwise stations should react locally, in a strip-theory or lifting-line sense, because noncompactness effects should then tend to concentrate unsteady airloads at the wing's leading edge. In the present study we remove this approximation. Now different wing sections are allowed to influence each other, and the computed airload at each point on the wing surface depends on that at every other point. The wing remains unswept and of constant chord. The model is applied to the Hamilton Standard propeller/Gulfstream II wing combination.

B. Propeller Wake Model and Wing Aerodynamics

1. Analysis of Downwash

Figure III.1 shows the wake model. Each vortex contributes a downwash field on the wing plane given by

$$\frac{\Gamma}{2\pi} \; \frac{\tilde{y}-\tilde{y}_o}{(\tilde{y}-\tilde{y}_o)^2+h_o^2}$$

with $\tilde{y}_o=R_t\cos\Omega t$, $h_o=R_t\sin\Omega t$; so that the total influence of the N straight, equally spaced vortices is

$$w(t,y) = \frac{\Gamma}{2\pi R_t} \sum_{k=1}^{N} \frac{y/\bar{R}-\cos[\Omega t+2\pi(k-1)/N]}{1+(y/\bar{R})^2-2(y/\bar{R})\cos[\Omega t+2\pi(k-1)/N]} \qquad \text{(III.1)}$$

where y and $\bar{R}$ stand for $\tilde{y}/b, R_t/b$, with wing semichord b assumed constant.

The analysis to obtain the corresponding harmonics begins with an identity involving two arbitrary complex numbers $\tau = e^{i\beta}$, $z = re^{i\alpha}$ (e.g., Ref. 14).

$$\frac{\tau}{\tau - z} + \frac{z^*}{\tau^* - z^*} = \frac{1-r^2}{1+r^2-2r\cos(\alpha-\beta)} \qquad \text{(III.2)}$$

where * denotes conjugate.

For r<1 we may now express the left hand side of Eq. III.2 as

$$1 + 2 \sum_{m=1}^{\infty} r^m \cos m(\alpha-\beta)$$

Since r, the magnitude of z, is by definition positive, this relationship is immediately applicable to the range $0<y/\bar{R}<1$. Thus, letting $y/\bar{R}=r$, $\Omega t=\alpha$, $-\beta = \frac{2\pi(k-1)}{N}$, and performing some algebra one finds that

$$\frac{y/\bar{R}-\cos[\Omega t + \frac{2\pi(k-1)}{N}]}{1+(y/\bar{R})^2-2(y/\bar{R})\cos[\Omega t+\frac{2\pi(k-1)}{N}]} = -\sum_{m=1}^{\infty} (y/\bar{R})^{m-1} \cos m[\Omega t+\frac{2\pi(k-1)}{N}] \qquad \text{(III.3)}$$

By a similar calculation for r>1 the left hand side of Eq. III.2 takes the form

$$-\left\{1+2 \sum_{m=1}^{\infty} \frac{\cos m(\alpha-\beta)}{r^m}\right\}$$

and for $1<y/\bar{R}<\infty$ we find that

$$\frac{y/\bar{R}-\cos[\Omega t + \frac{2\pi(k-1)}{N}]}{1+(y/\bar{R})^2-2(y/\bar{R})\cos[\Omega t + \frac{2\pi(k-1)}{N}]} = \sum_{m=0}^{\infty} \frac{\cos m[\Omega t + \frac{2\pi(k-1)}{N}]}{(y/\bar{R})^{m+1}} \qquad \text{(III.4)}$$

If the cosines on the right sides of Eqs. III.2 and III.4 are now expanded out, and the sum $\sum_k$ is interchanged with $\sum_m$, the following two factors appear

$$\sum_{k=1}^{N} \cos\left[\frac{2\pi m(k-1)}{N}\right] \;,\; \sum_{k=1}^{N} \sin\left[\frac{2\pi m(k-1)}{N}\right] \quad ;$$

the first of which is zero unless m is a multiple of N, and then it equals N. The second sum is identically zero. These conclusions may be used to find, for example, that the right side of Eq. III.3 becomes

$$-N \sum_{m=1} (y/\bar{R})^{Nm-1} \cos mN\Omega t$$

The simple manipulations used to obtain the series expression of w for $0<y<\infty$ may be adapted to the negative ranges $-1<y/\bar{R}<0$, $-\infty<y/\bar{R}<-1$. One writes

$$\frac{1-r^2}{1+r^2-2r\cos(\alpha-\beta)} = \frac{1-r^2}{1+r^2-2(-r)\cos(\alpha-\beta+\pi)}$$

and then replaces y by $-y>0$ and $\frac{2\pi(k-1)}{N}$ by $\frac{2\pi(k-1)}{N} + \pi$ in the previous results.

The final series representations for $w=w(t,-\infty<y<\infty)$ are found to be

$$w(t,y)=\frac{\Gamma N}{4\pi R_t}\left[\begin{array}{l} \displaystyle\sum_{m=-\infty}^{\infty} e^{imN\Omega t}\,\nu_m \left\{\begin{array}{ll} \left(\frac{\bar{R}}{y}\right)^{N|m|+1} & \bar{R}<y<\infty \\ (-1)^{N|m|+1}\left(\frac{\bar{R}}{-y}\right)^{N|m|+1} & -\infty<y<-\bar{R} \end{array}\right. \\ \text{and} \\ \displaystyle\sum_{m=-\infty}^{\infty} e^{imN\Omega t}(\delta_{om}-1) \left\{\begin{array}{ll} (y/\bar{R})^{N|m|-1} & 0<y<\bar{R} \\ (-1)^{N|m|-1}(-y/\bar{R})^{N|m|-1} & -\bar{R}<y<0 \end{array}\right. \end{array}\right. \qquad \text{(III.5)}$$

where $\nu_m=2$ or 1 for $m=0$, $m\neq0$, respectively; Kronecker delta δ_{om} equals 1 when $m=0$ and is zero otherwise. Identifying $w_{mN}(y)$ in the above, we have that

$$w_{mN}(y) = \frac{\Gamma N}{4\pi R_t} \left[\begin{array}{l} \nu_m \cdot \begin{cases} (\bar{R}/y)^{N|m|+1} & \bar{R}<y<\infty \\ (-1)^{N|m|+1}(\frac{\bar{R}}{-y})^{N|m|+1} & -\infty<y<-\bar{R} \end{cases} \\ \\ (\delta_{mo}-1) \begin{cases} (y/\bar{R})^{N|m|-1} & 0<y<\bar{R} \\ (-1)^{N|m|-1}(-y/\bar{R})^{N|m|-1} & -\bar{R}<y<0 \end{cases} \end{array} \right. \qquad \text{(III.6)}$$

As discussed in Ref. 11, it is of interest to note that the harmonic decomposition in Eq. III.5 yields a nonzero value for $w_o(|y|>\bar{R})$. This "static" component of downwash would affect the steady performance of the wing.

We shall need the spanwise Fourier transform

$$\bar{w}_{mN}(\lambda) = \int_{-\infty}^{\infty} dy\ e^{i\lambda y} w_{mN}(y) \qquad \text{(III.7)}$$

of the above; we obtain

$$\bar{w}_{mN}(\lambda) = \frac{\Gamma N}{2\pi R_t} \exp\{\frac{i\pi}{2}(N|m|+1)\}$$

$$\cdot \left[\frac{\nu_m \bar{R}^{N|m|+1}}{(N|m|)!} \left\{ \sum_{j=1}^{N|m|} \lambda^{j-1} \frac{(N|m|-j)!\cos[\lambda\bar{R}-\frac{\pi}{2}(N|m|-j+2)]}{\bar{R}^{N|m|-j+1}} - \frac{\lambda}{|\lambda|} \mathrm{si}(|\lambda|\bar{R}) \,.\, \lambda^{N|m|} \right\} \right.$$

$$\left. + \frac{(1-\delta_{mo})(N|m|-1)!}{\bar{R}^{N|m|-1}} \left\{ \sum_{j=1}^{N|m|-1} \frac{(\bar{R}^{N|m|-j}(-1)^{j+1}}{\lambda^j (N|m|-j)!} \cos[\lambda\bar{R}-\frac{\pi}{2}(N|m|+j-1)] + \frac{\sin\lambda\bar{R}}{\lambda^{N|m|}} \right\} \right] \qquad \text{(III.8)}$$

where si(z) is defined as[15]

$$\mathrm{si}(z) = -\int_z^{\infty} dt\, \frac{\sin t}{t}$$

The quantity in large square brackets is real; it is odd in λ for even values of mN and even in λ for odd mN. Since the exponential factor outside equals $(-1)^{(N|m|+1)/2}$ if Nm is odd and $i(-1)^{N|m|/2}$ for even Nm, it follows that in general

$$\bar{w}_{mN}(-\lambda) = \bar{w}^*_{mN}(\lambda) \qquad \text{(III.9)}$$

where * denotes complex conjugate, in agreement with the observation based on Fig. III.2, which shows $4\pi R_t w_N(y)/\Gamma N$ (i.e., m=1) for N even or odd, that

$$\bar{w}_{mN}(\lambda) = \begin{cases} i \int_{-\infty}^{\infty} dy\, \sin(\lambda y) w_{mN}(y) \text{ for Nm even or} & \text{(III.10a)} \\ \int_{-\infty}^{\infty} dy\, \cos(\lambda y) w_{mN}(y) \text{ for Nm odd} & \text{(III.10b)} \end{cases}$$

i.e., that Eq. III.10a is odd in λ while III.10b is even in λ.

2. Aerodynamic Response

The harmonics of the downwash distribution of a single propeller have been shown to be always odd about the propeller axis if the number of blades is even, and either even or odd (depending on whether Nm is odd or even) when the number of blades is odd.

The boundary-value problem for the perturbation velocity potential $\Phi(x,y,z,t)$ on the frame of reference of the wing is

$$\left(\frac{\partial^2}{\partial x^2} + \frac{\partial^2}{\partial y^2} + \frac{\partial^2}{\partial z^2}\right)\Phi - \frac{b^2}{c_o^2}\frac{D^2\Phi}{Dt^2} = 0 \text{ for all } x,y,z \qquad \text{(III.11)}$$

$$\frac{\partial \Phi}{\partial z}(0<x<2,y,o,t) = -w(t,y) \qquad \text{(III.12)}$$

$$\frac{D\Phi}{Dt}(x\geq 2,y,o,t) = 0 \qquad \text{(III.13)}$$

where c_o is sound speed and $D/Dt=\partial/\partial t+(U/b)\partial/\partial x; x,y,z$ have normalized by wing semichord b. We now let

$$\Phi(x,y,z,t) = \sum_{m=-\infty}^{\infty} \phi_{mN}(x,y,z)e^{imN\Omega t} \tag{III.14}$$

as required by Eq. III.5; also, with $\omega=mN\Omega$, $k=\omega b/U$, and $\mu=kM/\beta^2$, we let

$$\Phi_{mN}(x,y,z) = \Phi^*_{mN}(x,y,z)e^{i\mu Mx} \tag{III.15}$$

and obtain that

$$\frac{\partial^2\Phi^*_{mN}}{\partial x^2} + \frac{\partial^2\Phi^*_{mN}}{\partial(\beta y)^2} + \frac{\partial^2\Phi^*_{mN}}{\partial(\beta z)^2} + \mu^2\Phi^*_{mN} = 0 \tag{III.16}$$

$$\frac{\partial\Phi^*_{mN}}{\partial(\beta z)}(0<x<2,y,0) = -\frac{w_{mN}(y)e^{-i\mu Mx}}{\beta} \tag{III.17}$$

Finally, letting $\beta z=Z$ and

$$\Phi^*_{mN}(x,y,Z) = \int_{-\infty}^{\infty}\frac{d\lambda}{2\pi}\, e^{-i\lambda y}\, \bar{\Phi}^*_{mN}(x,Z;\lambda) \tag{III.18}$$

to conform with Eq. III.7, yields

$$\frac{\partial^2\bar{\Phi}^*_{mN}}{\partial x^2} + \frac{\partial^2\bar{\Phi}^*_{mN}}{\partial Z^2} + \tilde{\mu}^2\bar{\Phi}^*_{mN} = 0 \text{ all } x,Z \tag{III.20}$$

$$\frac{\partial\bar{\Phi}^*_{mN}}{\partial Z}(0<x<2,0) = -\frac{\bar{w}_{mN}}{\beta}e^{-i\mu Mx} \tag{III.21}$$

$$\left(\frac{ik}{\beta^2} + \frac{\partial}{\partial x}\right)\bar{\Phi}^*_{mN}(x\geq 2,0) = 0 \tag{III.22}$$

where

$$\tilde{\mu} = \sqrt{\mu^2-\lambda^2/\beta^2} = -i\sqrt{\lambda^2/\beta^2-\mu^2} \tag{III.23}$$

the latter equality actually being a consequence of the choice of branch cuts for $\omega>0$ to satisfy the radiation condition (for $\tilde{\mu}^2>0$ is assumed to have a small negative imaginary part which becomes large when $\tilde{\mu}^2<0$).

Since the propeller wake model uses straight vortices aligned with the flight direction, the induced downwash is constant across the wing chord. We now adapt an approximate solution by Amiet[5] for an airfoil in oscillatory plunging motion at high flight speed. Since Amiet has considered only the purely two-dimensional constant downwash problem , the expression for loading given below constitutes a generalization analogous to Adamczyk's[4] skewed-wing analysis for a convected gust. We write the final result for the y-transform of the pressure distribution on the lower surface of the wing:

$$\bar{p}_{mN}(0<x<2;\ z=0^-;\lambda) = \frac{\rho U \bar{w}_{mN}(\lambda)\,(1+i)}{\beta\sqrt{\tilde{\mu}^2-\mu^2M^2}}\ \cdot$$

$$\Big\{ kE^*[(\tilde{\mu}-\mu M)x] - i\sqrt{\frac{\tilde{\mu}-\mu M}{2\pi x}}\ \exp\{-i(\tilde{\mu}-\mu M)x\}$$

$$+ E^*[(\tilde{\mu}+\mu M)(2-x)] - \left(\frac{1-i}{2}\right)\Big\} \qquad \text{(III.24)}$$

from which we compute the surface pressure everywhere

$$p_{mN}(x,y,0^-) = \int_{-\infty}^{\infty} \frac{d\lambda e^{-i\lambda y}}{2\pi}\,\bar{p}_{mN}(x,0^-;\lambda) \qquad \text{(III.25)}$$

$$= \frac{\rho U\Gamma N}{\beta R_t}\,\frac{(1+i)}{2\pi^2}$$

$$\int_0^{\infty} \frac{d\lambda}{\sqrt{\tilde{\mu}^2-\mu^2M^2}} \Big\{ kE^*[(\tilde{\mu}-\mu M)x] - i\sqrt{\frac{\tilde{\mu}-\mu M}{2\pi x}}\ \exp\{-i(\tilde{\mu}-\mu M)x\}$$

$$+ E^*[(\tilde{\mu}+\mu M)(2-x)] - \left(\frac{1-i}{2}\right)\Big\}$$

$$.\mathrm{Re}\,\{\exp[\tfrac{i\pi}{2}(N|m|+1) - i\lambda y]\ \tilde{w}_{mN}(\lambda)\} \qquad \text{(III.26)}$$

where $\tilde{w}_{mN}(\lambda)$ stands for the quantity within large square brackets in Eq.III.8. Since $p_{mN}(-z)=-p_{mN}(+z)$ the actual loading, defined in the positive-lift sense as $p_{mN}(0-)-p_{mN}(0+)$, is therefore given by +2 times Eq. III.26. Also, for $m<0$ $p_{mN}=p^{*}_{(-mN)}$, where asterisk denotes conjugate.

The large-y behavior may be found by deforming the contour implicit in Eq. III.25, in λ space, from the real axis to the several branch points present in the integrand; thus, for example, for $y>0$ one could deform to the lower half plane to pick up contributions at $\lambda=+\mu\beta^2=kM=k_{ac}$, the normalized acoustic wavenumber $\omega b/c_o$ (from the $(\tilde{\mu}^2-\mu^2M^2)^{-1/2}$ factor) and at $\lambda=+\mu\beta$ (from a branch point of $\tilde{\mu}$). It is obvious that of these the $\lambda=\mu\beta$ point is clearly a weak contributor compared to $\lambda=k_{ac}$. As $|y|\to\infty$ a straightforward asymptotic analysis therefore indicates that $p_{mN}\sim\exp\{-ik_{ac}|y|\}$, a net acoustic wave having its "origin" within the area of strong aerodynamic action.

It is important to point out that solution III.24 violates the condition of zero pressure on the plane of the wing both ahead of the leading edge and along the wing wake; it is the result of constructing a preliminary solution which satisfies the downwash boundary condition over the entire plane, and then correcting, by cancellations, pressures both ahead and behind the wing. As discussed in Ref. 5, for the chordwise-constant downwash case these corrections are found simultaneously rather than sequentially, with an outcome that does not satisfy pressure continuity either forward or aft of the wing. More corrections would result in better approximations to the computed loading.

3. Estimation of Vortex Strength

The estimate of strength for blade-tip vortices is here based on the following model: We assume that all blade-bound vorticity beyond a chosen radial station rolls up into a single concentrated vortex (Fig. III.3). We may take this radial station as that where the sectional loading is maximum, although for our purposes even this is unnecessary. Assuming a simple triangular shape for the lift with a prescribed maximum value L_{max}, one obtains that

$$\frac{1}{2} L_{max} R_t = \left(\frac{T}{N}\right) \frac{1}{\cos\beta_t} \tag{III.27}$$

regardless of radial point where the maximum is assumed to occur; in the above T is total steady propeller thrust and β_t is an effective or average twist plus pitch angle. The term in parenthesis denotes each blade's contribution to total performance thrust.

Applying these ideas at the tip radial position, we next invoke the lifting-line relationship,

$$\rho\Gamma\sqrt{U^2+(\Omega R_t)^2} = L_{max} \tag{III.28}$$

from which finally we obtain that the leading factor in Eq. III.26 is

$$\frac{\rho U\Gamma N}{R_t} = \frac{T}{R_t^2} \cdot \frac{2}{\cos\beta_t} \cdot \frac{U}{\sqrt{U^2+(\Omega R_t)^2}} \tag{III.29}$$

suggesting that, for a given propeller design thrust T, lower pressures are obtained if the propeller radius is increased.

C. Application to Gulfstream-II Wing

For the Gulfstream-II we take b=7 ft (14-ft chord at engine location) and the total propeller thrust T at cruise as 1460 lb; $\beta_t=57^\circ$.[12] Flight Mach number M=.8; density and sound speed values correspond to an altitude of 35,000 ft. The results discussed below are for the fundamental frequency, 226 Hz, which at 35,000 ft has a wavelength of 4.3 ft.

Figures III.4-7 show predicted pressure distributions $p_N(x,y,z=0^-)$ over chords at $y=\bar{R}/2$, $\bar{R}$, $1.5\bar{R}$, and $4\bar{R}$. All results display the $1/\sqrt{x}$ leading-edge singularity. For most spanwise stations the singular region appears to be quite confined in extent, following one's expectations given the high speed/frequency of the situation ($\mu=28$). As earlier discussed, the nonzero values of loading computed along the trailing edge are an artifact of the approximate lifting-surface theory.

Figures III.8-10 are spanwise plots of $p_N(x, y>0, z=0^-)$ for chord stations x=.5, 1, 1.5 (quarter, half, and three-quarter chords). For $y<0$ the results would be inverted mirror images of those shown, due to the antisymmetry of loading about y=0 for an even number of blades. Point $4\bar{R}$ corresponds to a dimensional distance of 18' outboard of the propeller axis. The numerical solution displays the acoustic wavelength for large y in agreement with the discussion following Eq. III.26. The decay rate is $1/|y|$.

The most interesting feature of Figures III.8-10 is the smoothness of the aerodynamic response near $y=\bar{R}$ to an input downwash which is discontinuous there (cf. Fig. III.2a). The loading is generally nonzero at $y=\bar{R}$ because $y=\bar{R}$ is not a point of spanwise downwash antisymmetry. Neither of these observations would apply to the loading obtained from the strip-theory model, which requires that the spanwise behavior of the pressure be the same as that of the input downwash, which, incidentally, lacks the acoustic wavenumber at large distances from the origin. The input downwash is strictly hydrodynamic in nature, while the aerodynamic response to it should be definitely wavelike, or acoustic.

We have noted that for an even number of propeller blades all harmonics of spanwise loading p_{mN} are antisymmetric about the propeller axis in spanwise coordinate. All, therefore, contribute net moments which drive the wing as a whole at the engine station. Were it not for the fact that the frequency regime requires that plating response also be considered in detail, these loads could be applied in cruder models of wing motion.

When the number of blades is odd the fundamental distribution is even about the propeller axis, contributing a net lift. Higher harmonics are alternately odd and even, contributing either torques or forces.

D. Predicted Benefit of a Large Number of Blades in Reducing Unsteady Wing Airloads Induced by the Wake of an Upstream Propeller

The argument to demonstrate that for a given value of propeller performance thrust and aircraft lift unsteady wing airloads are reduced by a large number of blades will here parallel that in Section II.E.

Eqs. III.24 and 16 show that at high reduced frequency k (based on wing semichord and flight speed) induced wing pressure distributions are proportional to $\rho U\Gamma N/R_t \cdot k^{-1/2}$, where $\rho U\Gamma N/R_t$ is in turn proportional to T/R_t^2, with T denoting steady propeller thrust. Since for steady flight the amplitude coefficient of wing pressures may be interpreted as proportional to the product of the freestream dynamic pressure and a spanwise-variable lift coefficient, we have that for point x,y on the wing surface

$$\frac{p_{mN}}{p^{steady}} \propto \frac{T/R_t^2}{\rho U^2 c_L(y)} \cdot \frac{1}{\sqrt{k}} \qquad \text{(III.30)}$$

Moreover, since $k = mN\Omega b/U = mN(b/R_t)(\Omega R_t/U) \sim mN(b/R_t) \sim mN$, it therefore follows that for a given value of design thrust T unsteady wing pressures fall relative to steady pressures as $N^{-1/2}$, as N is increased.

APPENDIX A

JUSTIFICATION FOR EXCLUSION OF MULTIPLE-SCATTERING EFFECTS

A.1 INTRODUCTION

Two of our simplifying assumptions have been that the propeller blades effectively lay flat on their plane of rotation without pitch or twist, and that unsteady velocities mutually induced by unsteady components of blade-bound and shed-wake vorticity are negligible in comparison to incident modal velocity amplitudes.

The first assumption causes mutual influences through direct pressure fields to be identically zero because flat-plate loadings for each blade involve then only thrust dipoles normal to the propeller disk. We shall examine its validity by estimating the pressure field with which two neighboring blades insonify each other, given that in fact a finite angle of twist exists between them. The procedure will be to use the aerodynamic theory available for a single airfoil at zero pitch or twist, and then to tilt the resulting source distribution through the actual pitch angle to find non-zero values of near-field pressure at off-plane points occupied by two adjacent blades. The results will be normalized by the input disturbance pressure $\rho U w_{mN}$ corresponding to the mN^{th} harmonic of the incident velocity field, and their fractional value will represent the pressure field's measure of unsteady aerodynamic interference, or multiple scattering, between blades.*

Similarly, estimates of interference through induced flows will rely on the zero-pitch loading solution appropriately tilted according to pitch. The ratio of such results to the amplitude of the incident velocity's first harmonic (say) will indicate a-posteriori to what extent each blade's aerodynamic response can be expected to be independent of others'.

Fig. A.1 shows a "radial" view of two of the N blades at an arbitrary circumferential cross-section through the propeller. As stated above, we shall use blade loadings corresponding to passage at zero twist and pitch. We shall further simplify the calculation by considering only the leading-edge contribution of such loading and its associated pressure field, i.e., by taking the airfoil to have its trailing edge at infinity.

---

*Mutually induced pressures are not used as input conditions in rigid-airfoil aerodynamics; however, certain situations may require simple estimates of (cont.)

A.2 BLADE-BLADE AERODYNAMIC INTERFERENCE THROUGH DIRECT PRESSURE FIELDS

For the semi-infinite chord airfoil Ref. 14 gives the pressure field an arbitrary field point (near or far):

$$p(r,\theta,t) = -\rho U w_{mN} \frac{\cos[1/2 \tan^{-1}(\beta \tan\theta)]}{\beta\sqrt{\pi r(\mu+k_x/\beta^2)(1-M^2\cos^2\Lambda \sin^2\theta)^{1/2}}}$$

$$\cdot \exp[i\{\omega t-k_s s + \frac{k_x M^2 \cos^2\Lambda\cdot x}{\beta^2} -\pi/4-\mu r\}] \qquad (A.1)$$

where in the present application, we have that

$$k_x = k_{mN} b \cos\Lambda$$

$$\omega = \Omega mN$$

$$k_s s \doteq mN \sin^{-1} y/R \qquad (A.2)$$

$$\theta = \tan^{-1} z/x \quad , \quad r = \sqrt{x^2+z^2}$$

etc, with k_{mN}, b, and Λ all functions of radial position R. In Eq. A.1 $U=\Omega R, M=U/c_o$, $\beta = \sqrt{1-M^2\cos^2\Lambda}$ and w_{mN} are also functions of R; also, the θ range must be defined as $(0,2\pi)$. We drop the b-subscript on the blade-based coordinate system defined in Fig. II.3.

For m=1 (the blade-passage fundamental) we have applied Eq. A.1 to calculate airfoil A's pressure field at airfoil B's location, and vice-versa. The results normalized by $\rho w_N U$ are displayed in Fig. A.2 for three radial stations. The maximum interference pressure is shown to be about 16% $\rho U w_N$ for $R=R_{tip}$ for blade A on blade B. This result, based on an airfoil model which does not satisfy the Kutta condition and which in fact yields maximum pressures along the wake direction, should be a conservative estimate for the lower values of blade pitch near the blade tips. Unfortunately, a correcting trailing-edge solution to prove the above assertion by modifying Eq. A.1 to satisfy the Kutta condition is not available in closed form for arbitrary field points and, at any rate, the value of 16%

---

[*] total chordwise gradients as input, for example, to unsteady boundary-layer flow calculations. Another possible application is the total loading influence function as input in an aeroelastic calculation.

is sufficiently low to justify neglecting the forward-scatter from airfoil A on airfoil B. The broken lines in Fig. A.2 summarize the computed levels of normalized backscatter (airfoil B on A). As expected, they are for the most part significantly below the solid lines, not just because the spurious trailing-edge point is further away, but because compressibility effectively lengthens distances to upstream points (as well as enhances propagation downstream by washing it along). The effect is embodied in the argument of the cosine factor in Eq. A.1. Let us take, for example, two angular positions symmetric about the $\theta=\pi/2$ divide between upstream and downstream regions at zero pitch, say $\theta_1=45^\circ$ for downstream and $\theta_2=135^\circ$ for upstream. With $\beta=1$, i.e., without compressibility,* $\theta_1/2=22.5^\circ$ and $\theta_2/2=67.5^\circ$. With $\beta=1/2$ ($M=.866$ for $\Lambda=0$, however, $\tan^{-1}(\beta\tan\theta)$ becomes, respectively for θ_1, θ_2, $\tan^{-1} 1/2=26.6^\circ$ so that $1/2 \tan^{-1}(\beta\tan\theta)=13.3^\circ$, and $\tan^{-1}(-1/2)=153.4^\circ$ so that $1/2 \tan^{-1}(\beta\tan\theta)=76.7^\circ$. Compressibility has therefore increased the difference between upstream and downstream signal amplitudes from $M=0$: $\cos(22.5^\circ)-\cos(67.5^\circ)=.924-.383=.54$, to $M=.866$: $\cos(13.3^\circ)-\cos(76.7^\circ)=.973-.230=.74$.

In principle Eqs. A.1 and II.21, etc., hold up to supersonic Mach number sec Λ, when sweep is present.

---

* It is important to remember that the model of the airfoil with semi-infinite chord becomes irrelevant at $M=0$ for the special case of zero blade sweep, and that it is useful in the so-called hyperbolic regime only when the frequency and Mach number are both high enough to yield certain minimum values of μ and k_x/β^2. (cf. Ref. 5's skewed-gust analysis).

A.3 BLADE-BLADE AERODYNAMIC INTERFERENCE THROUGH INDUCED FLOWS

The potential Φ associated with the pressure field of Eq. A.1 is obtained from Bernoulli's equation

$$\frac{D\Phi}{Dt} = -\frac{p}{\rho} \tag{A.3}$$

where D/Dt is the linearized substantial derivative $\partial/\partial t+(U/b)\partial/\partial x$. The solution of Eq. A.3 is conveniently expressed in terms of contour integral C(Fig. A.2a)

$$\Phi(x,s,Z,t) = \frac{ibw_{mN}}{2\pi\beta}\frac{1}{\sqrt{\zeta}}\cdot\frac{Z}{|Z|}$$

$$\cdot\exp[i\{\omega t-k_s s+k_x M^2\cos^2\Lambda x/\beta^2\}]$$

$$\cdot\int_C \frac{d\lambda\ \exp\{-i\lambda x-|Z|\sqrt{\lambda^2-\mu^2}\}}{\sqrt{\lambda-\mu}\ (\lambda-k_x/\beta^2)} \tag{A.4}$$

where in the present context ω, k_x, k_s, etc are as given by Eqs. A.2. Z is the nondimensional normal to airfoil coordinate compressed by the β factor, i.e., $Z=\beta z$; ζ is shorthand for $\mu+k_x/\beta^2$.

Differentiating with respect to zb we obtain the ratio of induced vertical velocity $w^i(x,s,Z)$ to incident velocity harmonic w_{mN} at field point x,Z.

$$\frac{w^i(x,s,Z,t)}{w_{mN}} = -\frac{i}{2\pi}\frac{1}{\sqrt{\zeta}}\exp[i\{\omega t-k_s s+k_x M^2\cos^2\Lambda x/\beta^2\}]$$

$$\int_C \frac{d\lambda\sqrt{\lambda+\mu}\ \exp\{-i\lambda x-|Z|\sqrt{\lambda^2-\mu^2}\}}{\lambda-k_x/\beta^2} \tag{A.5}$$

If we let Z=0 and take x>0, Eq. A.5 yields

$$\frac{w^i(x>0,s,z=0,t)}{w_{mN}} = -\exp[i\{\omega t-k_s s-k_x x\}] \tag{A.6}$$

as required by the boundary condition of flow tangency on the semi-infinite chord extending over $0<x<\infty$. For $x<0$, $Z=0$, the branch point contribution (Fig. A.2b) from $\lambda=-\mu$ gives the vertical velocities induced upstream on the plane of the blade:

$$\frac{w^{i}(x<0,s,z=0,t)}{w_{mN}} = -\exp[i(\omega t-k_x x-k_s s)] \left\{ 1-(1+i)E^{*}[\zeta(-x)] - \frac{\exp[-i\{\pi/4+\zeta(-x)\}]}{\sqrt{\pi\zeta(-x)}} \right\} \qquad (A.7)$$

For large values of $-x$, i.e., far upstream, and specializing to the case of zero sweep so that $\mu=k_x M/\beta^2=kM/\beta^2$, the above becomes proportional to

$$\frac{\exp\left[\frac{ikM}{1-M}\{x+(1-M)\frac{c_o t}{b}\}\right]}{[\zeta(-x)]^{3/2}}$$

indicating a quickly decaying signal of very short wavelength as $M\to 1^-$ travelling at speed $-(1-M)c_o$ relative to the airfoil ($-c_o$ relative to the freestream). In Eq. A.7 the vertical induced velocity becomes infinite as $x\to 0^-$ because at $x=0^+$ the blade-bound vorticity has an infinite value.

Eq. A.7 could by itself be used to estimate upstream flows induced by blade B on A if one neglects the pitch angle so that the two blades are coplanar; small values of $|w^{i}(x<0,0,t)/w_{mN}|$ over the chord of A would then justify basing flow tangency on incident velocity alone as far as upstream influences are concerned. Here, however, we are also interested in potentially stronger shed-wake effects, and for this reason will keep the two airfoils at nonzero pitch.

In calculating the shed wake a choice must be made for the model of loading on an airfoil of finite chord. Here we choose that given by Eq. A.1 $\theta=0$ and corresponding to the leading-edge solution, but applied only over $0<x<2$. For $x>2$ the wake condition of $p=0=(\Delta p)$ will be enforced. At sufficiently high frequency or subsonic Mach number, the trailing-edge correction to such a loading has the relatively unimportant local effect of "rounding off" the resulting pressure discontinuity at $x=2$ by providing it with the proper $\sqrt{2-x}$ decay as $x \to 2^-$. For simplicity of notation and analysis we neglect sweep effects and take $k_x = k$ $(\Lambda \equiv 0)$.

The calculation can proceed along the lines of the analysis for the upstream influence by considering the singular structure of the velocity's λ-transform, or can instead begin by posing Possio's integral[17] for a point in the wake. For the sake of variety we take up the latter approach:

$$w^s(x,z=0,t) = -\frac{k}{\rho U}\int_0^2 d\xi \, \Delta p(\xi,t) K(|x-\xi|) \tag{A.8}$$

with $K(|x-\xi|)$ given by

$$K(x-\xi) = \frac{1}{4\beta}\left\{ e^{i\mu M(x-\xi)}\left(iM\, H_1^{(2)}[\mu(x-\xi)] - H_o^{(2)}[\mu(x-\xi)]\right) + i\beta^2 e^{-ik(x-\xi)} \int_{-\infty}^{k(x-\xi)/\beta^2} du\; e^{iu} H_o^{(2)}(M|u|) \right\} \tag{A.9}$$

after normalization by the semichord b and noting that $|x-\xi| = x-\xi$ for $x>2$ (the wake). The superscript s on $w^s(x)$ stands for shed wake. In Eq. A.8, Δp is given by $p^+ - p^- = 2p^+$ or twice the result in Eq. A.1 with $\theta=0$, $0<r=x<2$:

$$\frac{w^s(x,z=0,t)}{w_{mN}} = (1-i)\sqrt{\frac{2k}{(1+M)\pi}}\; e^{i\omega t}\int_0^2 \frac{d\xi}{\sqrt{\xi}}\, e^{-i\mu(1-M)\xi} K(x-\xi) \tag{A.10}$$

Incidentally, the upstream result in Eq. A.7 for a semi-infinite chord airfoil can also be obtained from Possio's integral applied for $x<0$. Then we would have that

$$x<0: \quad \frac{w^i(x,z=0,t)}{w_{mN}} = (1-i)\sqrt{\frac{2k}{(1+M)\pi}}\; e^{i\omega t}\int_0^\infty \frac{d\xi}{\sqrt{\xi}}\, e^{-i\mu(1-M)\xi} K(|x-\xi|) \tag{A.11}$$

where $K(|x-\xi|)$ is now given by

$$K(\xi-x) = \frac{1}{4\beta}\left\{ e^{i\mu M(x-\xi)}\left(-iM\, H_1^{(2)}[\mu(\xi-x)]-H_o^{(2)}[\mu(\xi-x)]\right)\right.$$

$$\left. + i\beta^2\, e^{-ik(x-\xi)}\int_{-\infty}^{k(x-\xi)/\beta^2} du\, e^{iu}\, H_o^{(2)}(-Mu)\right\} \qquad (A.12)$$

In Eq. A.11 the integral extends to infinity because the leading-edge loading has not been cut off past x=2 as required by $\Delta p(x>2, z=0, t)=0$ -- the wake condition implicitly applied in Eq. A.10.

We begin by looking at points far downstream from the trailing edge in terms of wavelengths and later examine in what sense the far wake so computed can be expected to hold closer to the trailing edge, given the contemplated high reduced frequencies and moderate-to-high subsonic Mach numbers. We approximate the Possio kernel by its large kx behavior. Thus,

$$i\beta^2 e^{-ik(x-\xi)}\int_{-\infty}^{k(x-\xi)/\beta^2} du\, H_o^{(2)}(M|u|)\, e^{iu}$$

$$= i\beta^2\, e^{-ik(x-\xi)}\left\{\frac{2i}{\beta} - \int_{k(x-\xi)/\beta^2}^{\infty} du\, H_o^{(2)}(Mu)\, e^{iu}\right\}$$

$$\sim -\, 2\beta e^{-ik(x-\xi)}\left\{1-\sqrt{\frac{1+M}{2M}}\,\left[1-(1-i)E\,\left\{\frac{k}{1+M}\,(x-\xi)\right\}\right]\right\}$$

$$-2\beta e^{-ik(x-\xi)} + e^{-i\mu(1-M)(x-\xi)}\left\{\frac{(1+i)(1+M)}{\sqrt{\pi\mu(x-\xi)}} + O(\mu^{-3/2})\right\} \qquad (A.13)$$

Similarly, for $\mu(x-\xi)>>1$ we have that

$$e^{i\mu M(x-\xi)}\{iM\, H_1^{(2)}[\mu(x-\xi)]-H_0^{(2)}[\mu(x-\xi)]\}$$

$$\sim e^{-i\mu(1-M)(x-\xi)}\left\{-\frac{(1+i)(1+M)}{\sqrt{\pi\mu(x-\xi)}}+O(\mu^{-3/2})\right\} \qquad \text{(A.14)}$$

which cancels the second term on the right side of Eq. A.13 so that

$$K(x-\xi)\underset{\mu(x-\xi)\to\infty}{=}-1/2\; e^{-ik(x-\xi)}+O\{\mu(x-\xi)\}^{-3/2}\cdot\exp\{-\frac{ikM}{1+M}(x-\xi)\} \qquad \text{(A.15)}$$

Substituting Eq. A.15 into A.10 we finally have that

$$\lim_{kx\to\infty}\frac{w^s(x,z=0,t)}{w_{mN}}\sim-(1-i)E\left(\frac{2k}{1+M}\right)e^{-ik(x-Ut/b)} \qquad \text{(A.16)}$$

The exponential factor in Eq. A.16 carries the obvious physical interpretation that the wake is convected and thus steady in the still fluid (for which the nondimensional x-coordinate becomes $x_s=x-Ut/b$). As $2k/(1+M)\to\infty$ (recalling that the 2 stands for nondimensional chord) we have that

$$w^s(x,z=0,t)\underset{kx\to\infty}{=}-e^{-ik(x-Ut/b)}\{1+O(k^{-1/2})\} \qquad \text{(A.17)}$$

This initially surprising result states that at high frequencies the "inviscid" far wake shed by an airfoil continues to cancel the vertical velocity of the input gust. In a more general high-speed context, it suggests the possibility of effectively nulling out for a chosen streamline the normal velocity component of an undesirable convected disturbance through the introduction of an airfoil.

There is yet another path to Eq. A.16 which although perhaps analytically less self-contained is at the same time physically more revealing. We write the integral equation for the strength $\gamma(x_s)$ of the vortex sheet in the far wake in the frame of reference of the still fluid:

$$w^s(x_s)=-\frac{1}{2\pi}\fint_{-\infty}^{\infty}\frac{d\xi\,\gamma(\xi)}{x_s-\xi} \qquad \text{(A.18)}$$

where the integral equation is of the Cauchy-Principal Value type and is so designated. The kernel $[-2\pi(x_s-\xi)]^{-1}$ solves the Laplace equation and is the usual special case of Biot-Savart's Law applied to the self-induced normal velocity field; it may be obtained from the Possio kernel for zero frequency and Mach number.

Fourier transforming Eq. A.18, recognizing that

$$\frac{1}{x_s-\xi} = \frac{i}{2}\int_{-\infty}^{\infty} d\lambda\, \frac{\lambda}{|\lambda|}\, e^{-i\lambda(x_s-\xi)} \tag{A.19}$$

and that $\bar{w}(\lambda)=FT\{w^s(x_s)\}$ is proportional to $\delta(\lambda-k)$, we therefore have that

$$\bar{\gamma}(\lambda) \sim 4\pi i\, \frac{\lambda}{|\lambda|}\, \delta(\lambda-k) \tag{A.20}$$

from which

$$\gamma(x_s) = 2iw^s(x_s) \Rightarrow iw^s=u^+ \tag{A.21}$$

since $\gamma=u^+-u^-=2u^+$, where $u^{+,-}$ denote tangential velocities just above and and below the shed wake.

Returning now to the airfoil's frame of reference we recall that application of $p=\Delta p=0$ along the wake requires that

$$\frac{D\Phi}{Dt}(x>2,o,t)=0 \tag{A.22}$$

whose solution is

$$\Phi(x,o,t) = \Phi\left(x=2,o,t-\frac{(x-2)b}{U}\right) \tag{A.23}$$

since $\Phi(x<0,o,t)\equiv 0$. With $\Phi(x,o^+,t)=\tilde{\Phi}(x,o^+)\exp(i\omega t)$ Eq. A.22, however, states that

$$i\omega\tilde{\Phi}(x,o)e^{i\omega t}=-\frac{U}{2}\gamma(x,t) \tag{A.24}$$

which via Eqs. A.23 and A.21 yields

$$\gamma(x,t) = \frac{-2ik}{b} \cdot \tilde{\Phi}(2,o) \; \exp\{ i\omega [t-(x-2)b/U]\} \qquad (A.25)$$

$$w^s(x,t) = -\frac{k\tilde{\Phi}(2,o)}{b} \; \exp\{i\omega [t-(x-2)b/U]\} \qquad (A.26)$$

Now, in Ref. 5 Eq. 15 Amiet has calculated $\tilde{\Phi}(x,o)$ to be

$$\tilde{\Phi}(x,o) = (1-i)E(\frac{kx}{1+M}) \frac{e^{-ikx}}{k} bw_{mN} \qquad (A.27)$$

and so we finally obtain that

$$w^s(x,t) = -w_{mN}(1-i)E(\frac{2k}{1+M}) \; \exp\{ i\omega [t-xb/U]\} \qquad (A.28)$$

thus reproducing Eq. A.16, which we now see is the result of two physically cancelling effects. On the one hand we have the k^{-1} loss of lift at high frequencies displayed by Eq. A.27 ($\tilde{\Phi}(2,o)$ is 1/2 the total airfoil bound circulation); on the other we have the linear dependence on frequency of the rate of vortex shedding as shown by Eqs. A.24-26.

For very high frequencies far-wake vertical motions have been found in Eq. A.17 to be identical to those self induced by the semi-infinite loading of Eq. A.1. The obvious conclusion is that given a willingness to neglect the effects of the near wake, which is reduced in both strength and extent with increasing frequency, we may take the solution of Eq. A.1 to model the vertical velocity distribution over $-\infty < x < \infty$, z=0 for an actual airfoil of finite chord. Again, the essential sin committed is omission of an additional effective origin introduced by the near wake in the vicinity of $x=2^+$. We justify it by reasoning that next to the infinite discontinuity in normal velocity across $x=0^{\pm}$ shown by Eqs. A.6,7 the neglected source should be comparatively unimportant.

Reintroducing sweep, in a form suitable for computation (removing the $1/\sqrt{-x}$ singularity), mutually induced normal velocities for airfoils A and B are given by

$$\frac{w^i(x,z,t)}{w_{mN}} = \exp\{ i(\pi/2+k_x M^2 \cos^2\Lambda x/\beta^2 - k_s s+\omega t)\} \mu\beta |z| .$$

$$\int_0^\infty d\xi \left\{ \frac{\xi H_1^{(2)}\left(\mu\sqrt{(x-\xi^2)^2+(\beta z)^2}\right)}{\sqrt{(x-\xi^2)^2+(\beta z)^2}} \, e^{-ik_x\xi^2/\beta^2} + \frac{H_1^{(2)}\left(\mu\sqrt{(x+\xi^2)^2+(\beta z)^2}\right)}{\sqrt{(x+\xi^2)^2+(\beta z)^2}} \, e^{ik_x\xi^2/\beta^2} \left[\xi\{1-(1+i)E^*(\zeta\xi^2)\} - \frac{\exp\{-i(\pi/4+\zeta\xi^2)\}}{\sqrt{\pi\zeta}}\right]\right\} \tag{A.29}$$

When calculating the influence of A on B, x=0 is at A's leading edge; for that of B on A, x=0 is at B's leading edge. In both calculations $|z|$ is the blade-blade vertical separation given by $(2\pi R/bN)\sin\beta_t$.

Fig. A.3 shows predicted induced velocities based on Eq. A.29. As expected they are more pronounced for A on B than vice-versa, with an overall high in amplitude ratio of roughly 14%. We conclude that for the present situations interference through induced flows is negligible by about the same margin as direct pressure fields.

REFERENCES

1 D.B. Hanson, "Compressible Helicoidal Surface Theory for Propeller Aerodynamics and Noise," AIAA J., Vol. 21, No. 6, June 1983, pp. 881-889.

2 M.T. Landahl, Unsteady Transonic Flow, Pergamon Press, 1961, pp. 73-75.

3 M.R. Myers and E.J. Kerschen, "Effect of Airfoil Camber on Convected Gust Interaction Noise," AIAA Paper 86-1873, 10th Aeroacoustics Conference, Seattle WA, July 9-11, 1986.

4 J.J. Adamczyk, "The Passage of an Infinite Swept Airfoil Through an Oblique Gust," NASA CR-2395, May 1974.

5 R.K. Amiet, "High Frequency Thin-Airfoil Theory for Subsonic Flow," AIAA J., Vol. 14, No. 8, August 1976, pp. 1078-1082.

6 D.S. Weir, "Wing Loads Induced by a Propeller Wake," AIAA Paper 86-1967, 10th Aeroacoustics Conf., Seattle WA, July 9-11, 1986.

7 H. Schlichting, Boundary Layer Theory, McGraw-Hill, 7th Ed., 1979, p. 734.

8 H. Ashley and M.T. Landahl, Aerodynamics of Wings and Bodies, Addison-Wesley, 1965, pp. 90-93.

9 R. von Mises, Theory of Flight, Dover, 1959, pp. 117-8.

10 M. Van Dyke, Perturbation Methods in Fluid Mechanics, Academic Press, 1964, cf. eqs. 4.11 p. 50 and eq. 4.62 p. 72. Even though one is uniformly valid on the airfoil and the other is not, both yield the same correct result at distances upstream large in terms of nose radius.

11 M.C. Junger, J.M. Garrelick, R. Martinez, and J.E. Cole, III "Analytical Model of the Structureborne Interior Noise Induced by a Propeller Wake," NASA CR 172381, May 1984.

12 J.C. Hardin and J.P. Mason, "A New Look at Sound Generation by Blade/Vortex Interaction," Journal of Vibration, Acoustics, and Reliability in Design, Transactions of the ASME, 224, Vol. 197, April 1985.

13 I. Lindblad,"The Effect on Acoustic Radiation of Mutual Interaction between a Line Vortex and an Airfoil," M.S. Thesis, Aeronautics Dept., Massachusetts Institute of Technology, May 1983.

14 G.F. Carrier, M. Krook, and C.E. Pearson, Functions of a Complex Variable, McGraw-Hill, 1966, p. 47.

15 M. Abramowitz and I. Stegun, Handbook of Mathematical Functions, Dover, 1964, p. 232, Eq. 5.2.26.

16 R. Martinez, S.E. Widnall, "An Aeroacoustic Model for High-Speed, Unsteady Blade-Vortex Interaction," AIAA Journal, Vol. 21, No. 9, pp. 1225-1231.

17 R.L. Bisplinghoff, H. Ashley, and R.L. Halfman, Aeroelasticity, Addison Wesley, 1955, pp. 324-5.

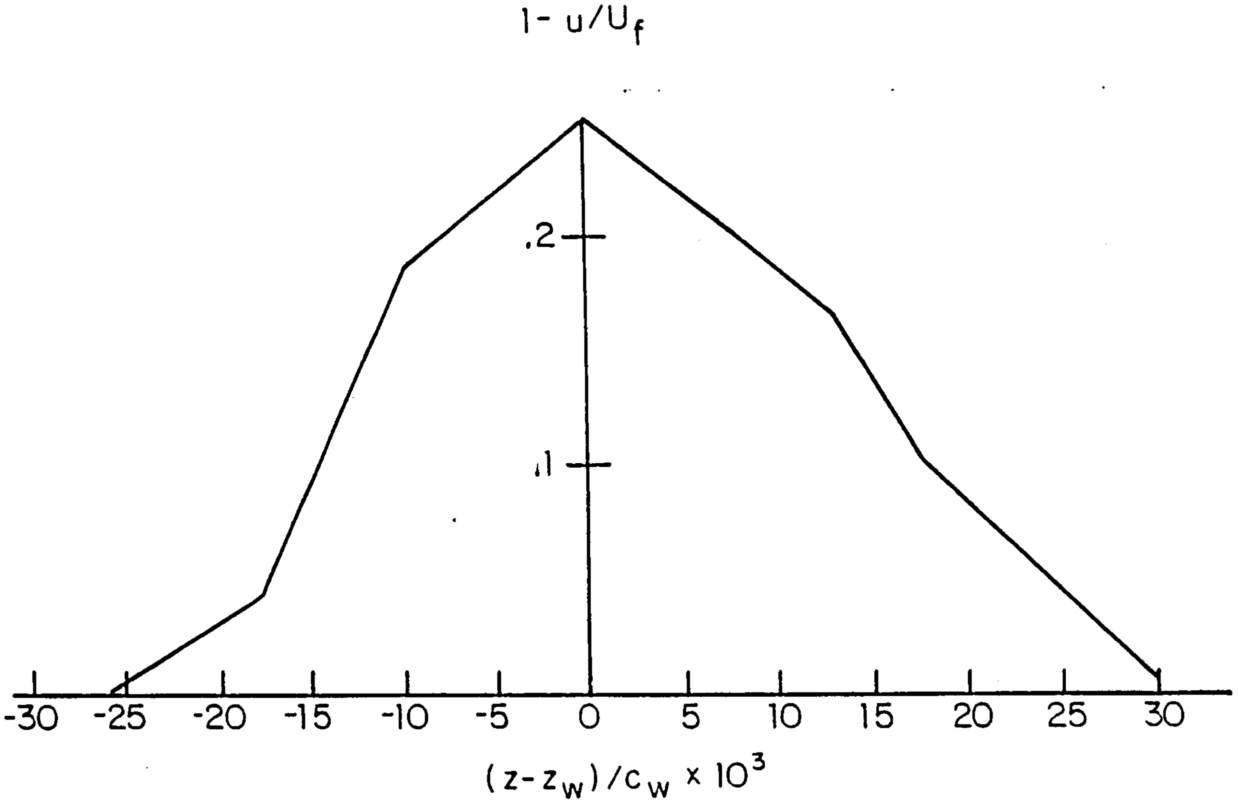

Fig. II.1 Mean wake measured at 32%-chord range downstream of the trailing edge of a typical full-scale aircraft. (courtesy of Douglas Aircraft Co.)

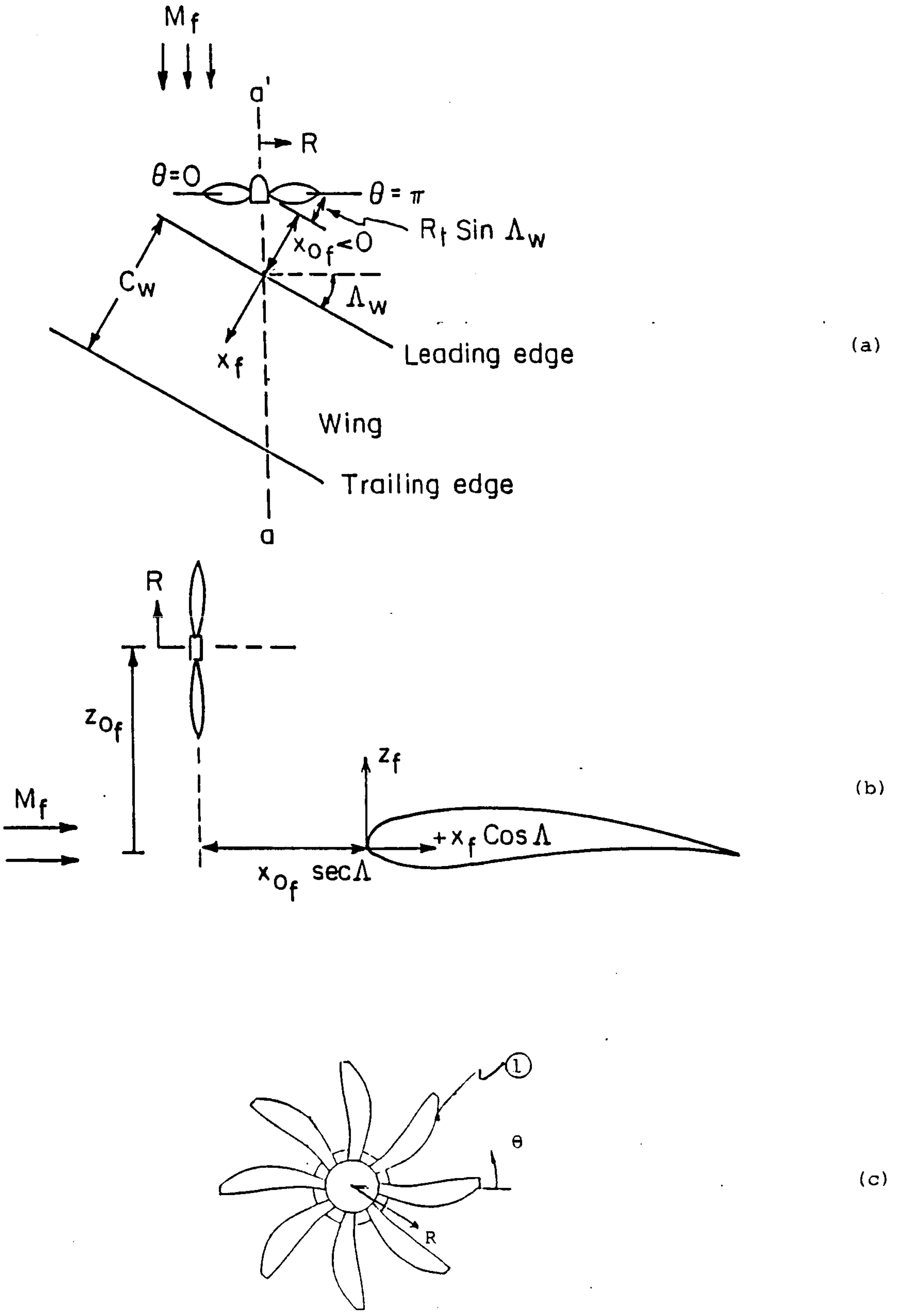

Fig. II.2 Idealization for wing interference model (a,b);and coordinate system for propeller blade aerodynamic analysis (cf. Fig. II.3 for expanded view of blade point ①).

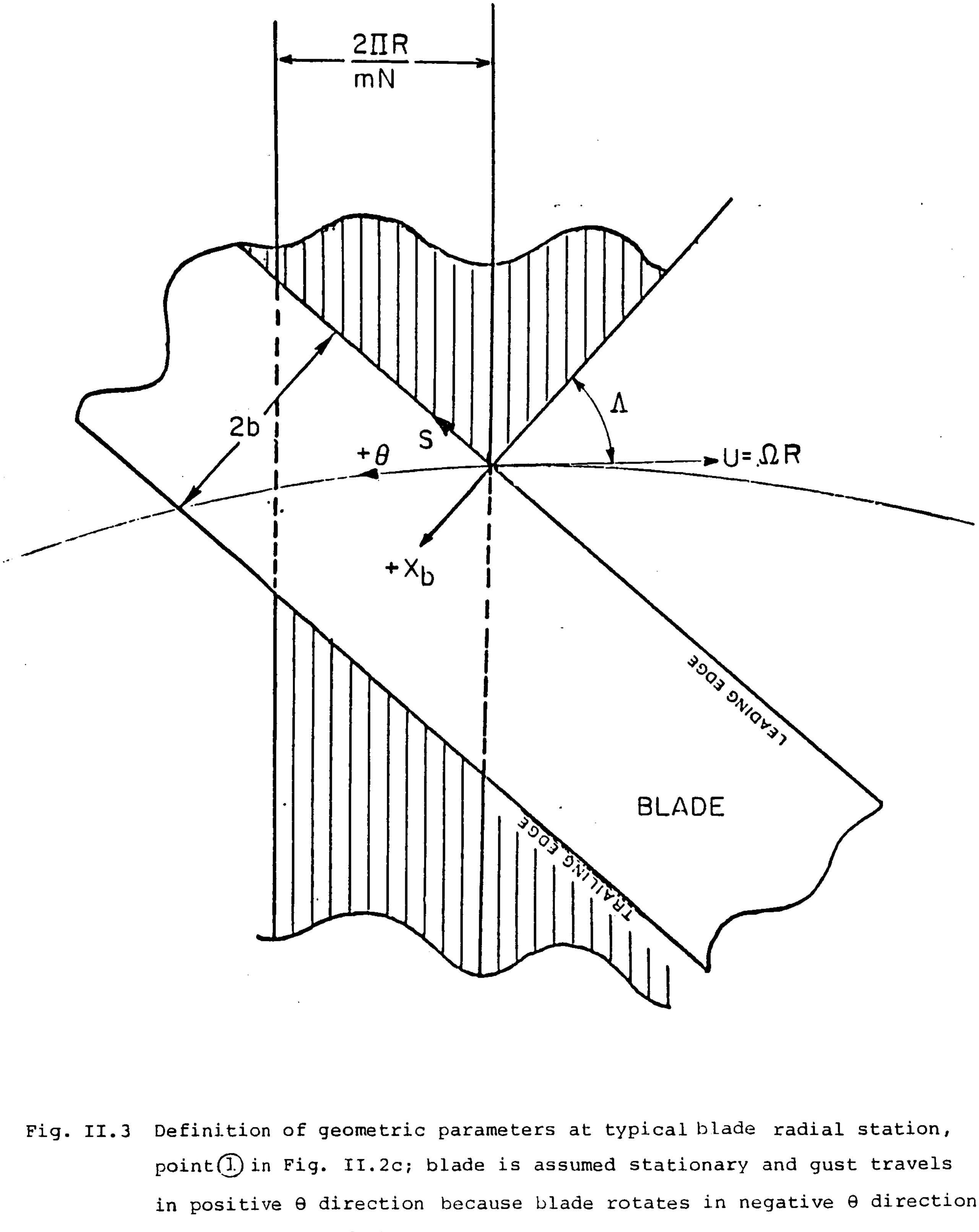

Fig. II.3 Definition of geometric parameters at typical blade radial station, point ① in Fig. II.2c; blade is assumed stationary and gust travels in positive θ direction because blade rotates in negative θ direction (adapted from Ref.4).

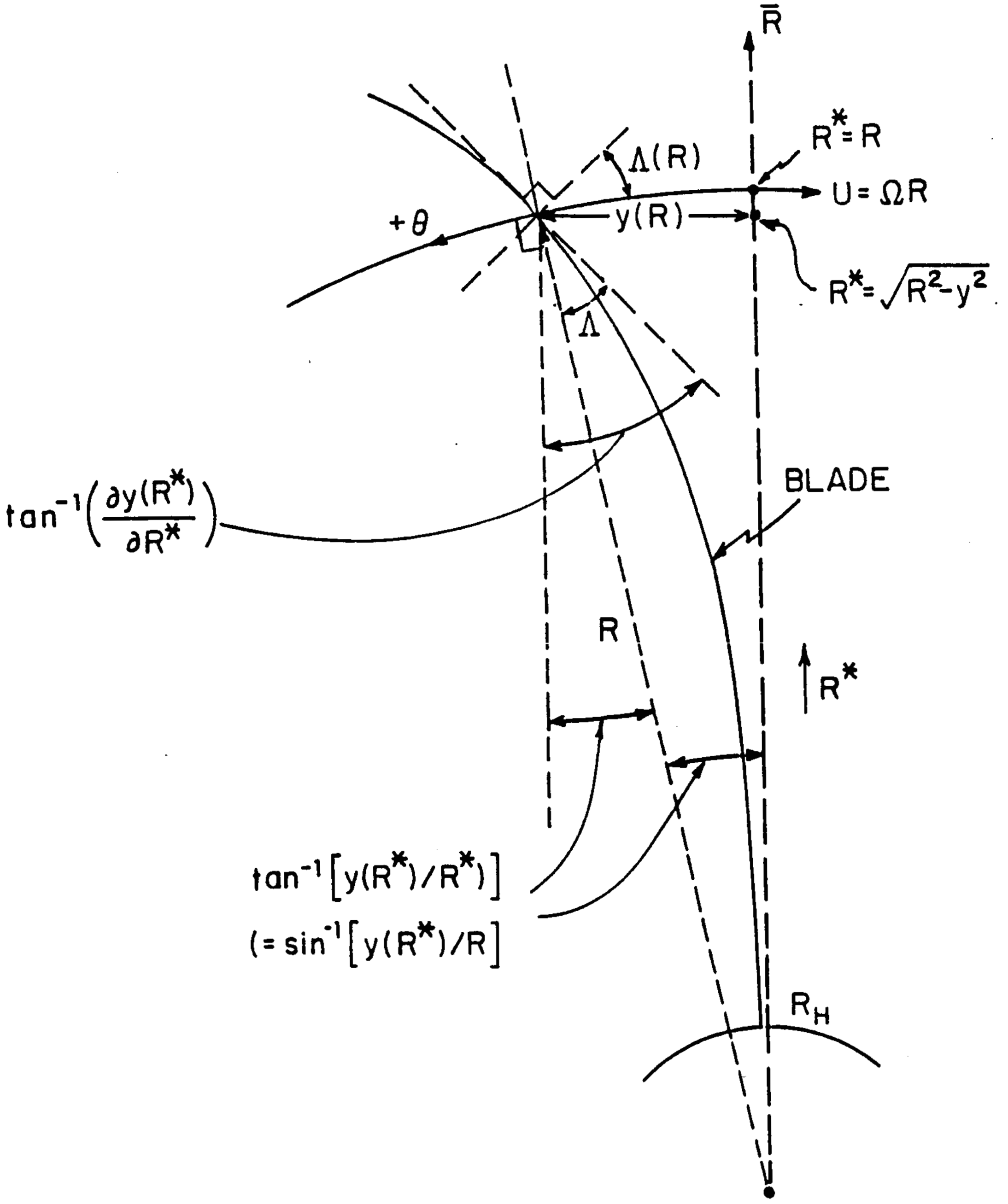

$$\Lambda(R) = \Lambda(\sqrt{R^{*2} + y^2}) = \tan^{-1}\left[\partial y(R^*)/\partial R^*\right] - \tan^{-1}\left[y(R^*)/R^*\right]$$

Fig. II.4 Schematic of modeled mean-sweep line for a blade, showing definitions of sweep and other parameters; global version of Fig. II.3.

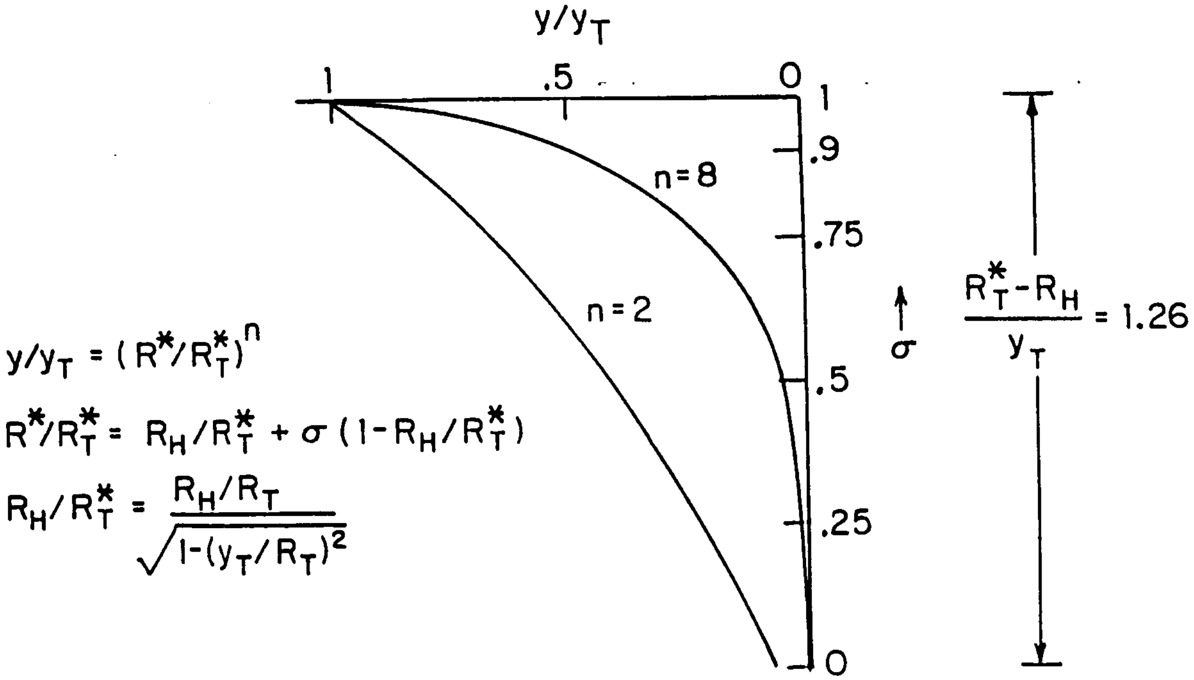

Fig. II.5 Mathematical model of family of blade-sweep lines, one for each value of power n, using $y_t/R_t=1/2$, $R_h/R_t=1/4$.

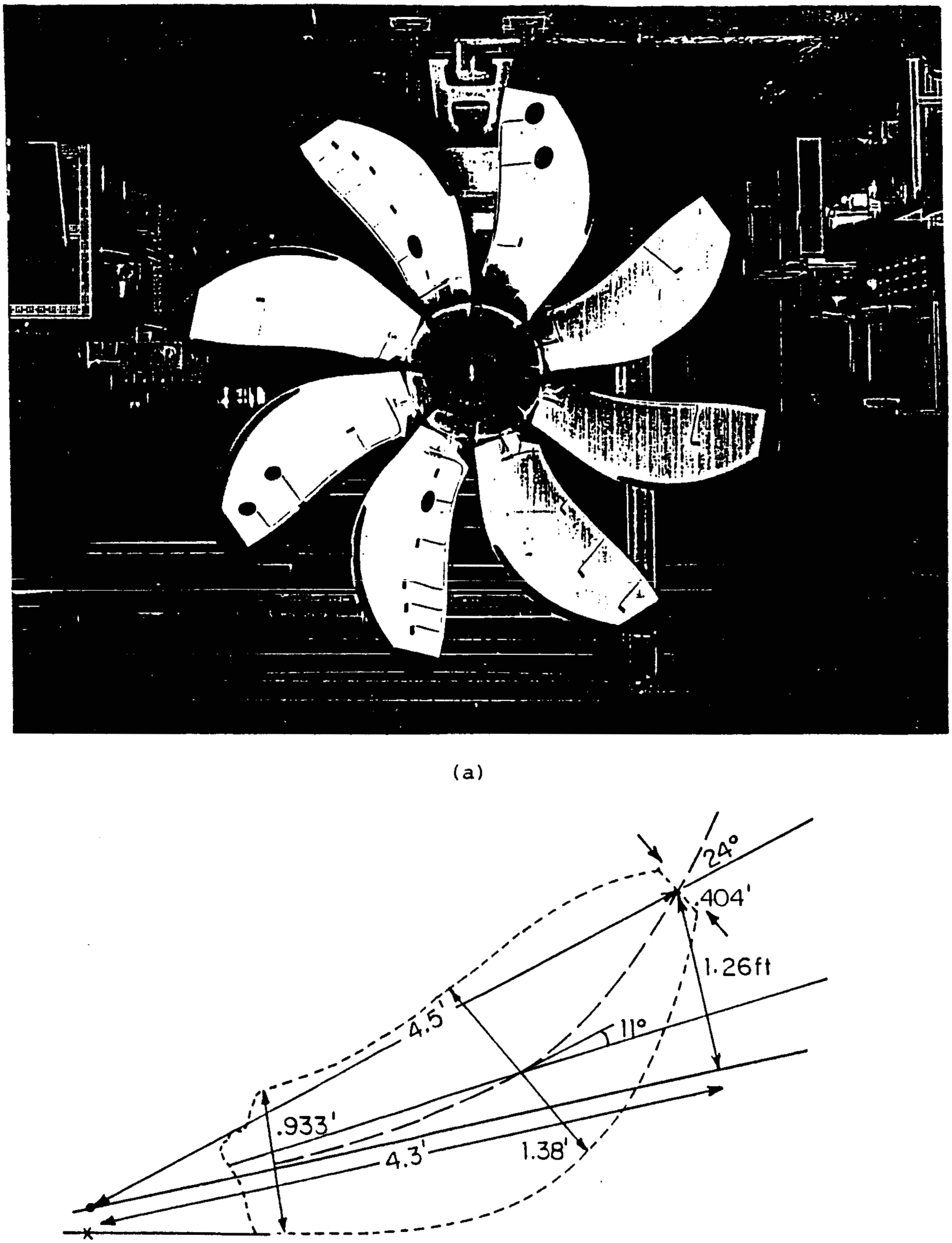

(a)

(b)

Fig. II.6 (a) Frontal view of full-scale propfan prototype;
(b) Expanded view of one of its blades indicating approximate circumferential dimensions and circumferential components of blade sweep angle.

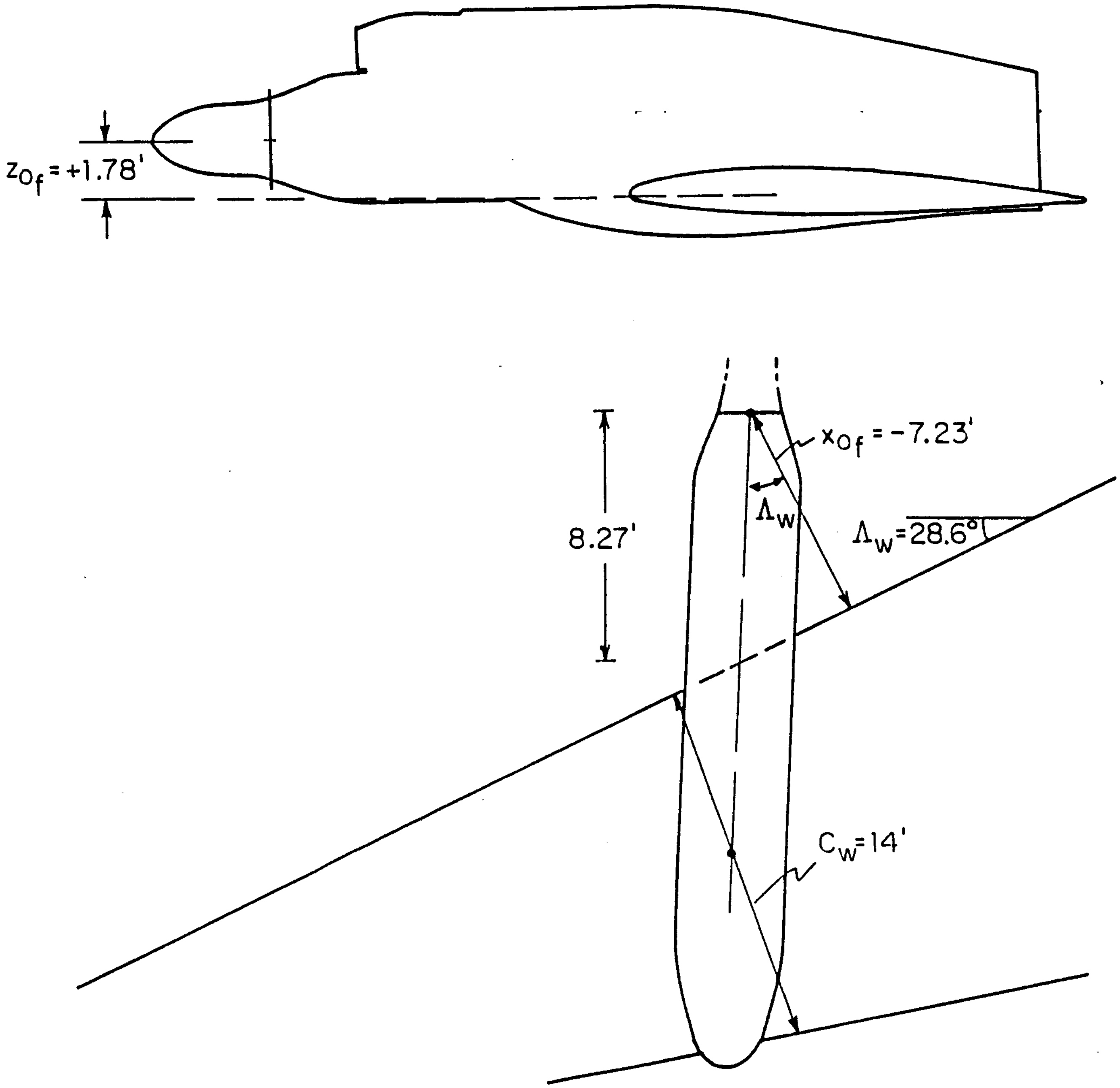

Fig. II.7 Top and side views of Gulfstream II wing and nacelle showing dimensions relevant to calculations.

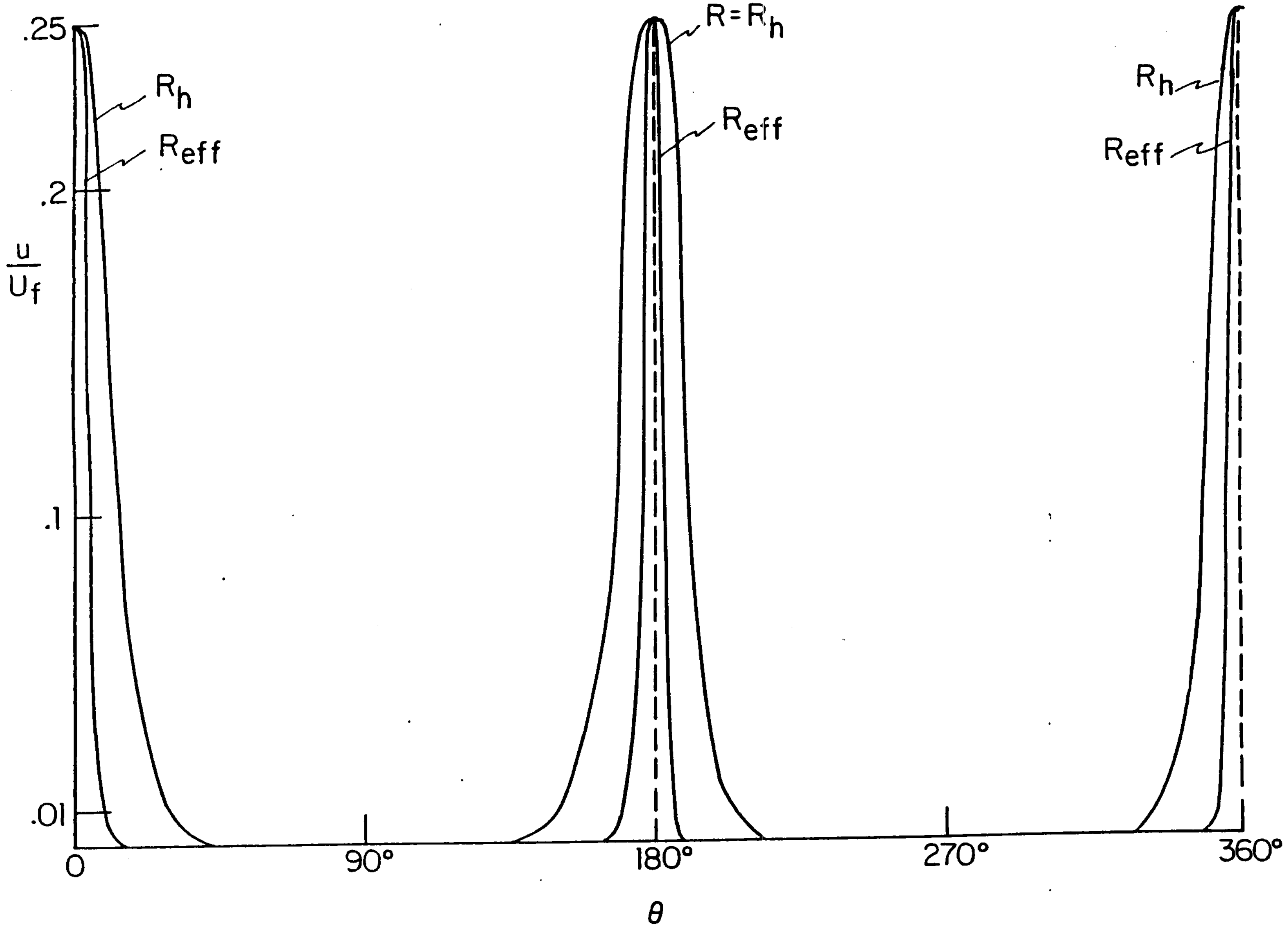

Fig. II.8 Modelled circumferential history of wing wake velocity deficit for two radial stations R_h, R_{eff_o} (based on measurements); propeller axis lies on wing plane, $z_{o_f}=0$. For pylon wake only the 180° spike is used.

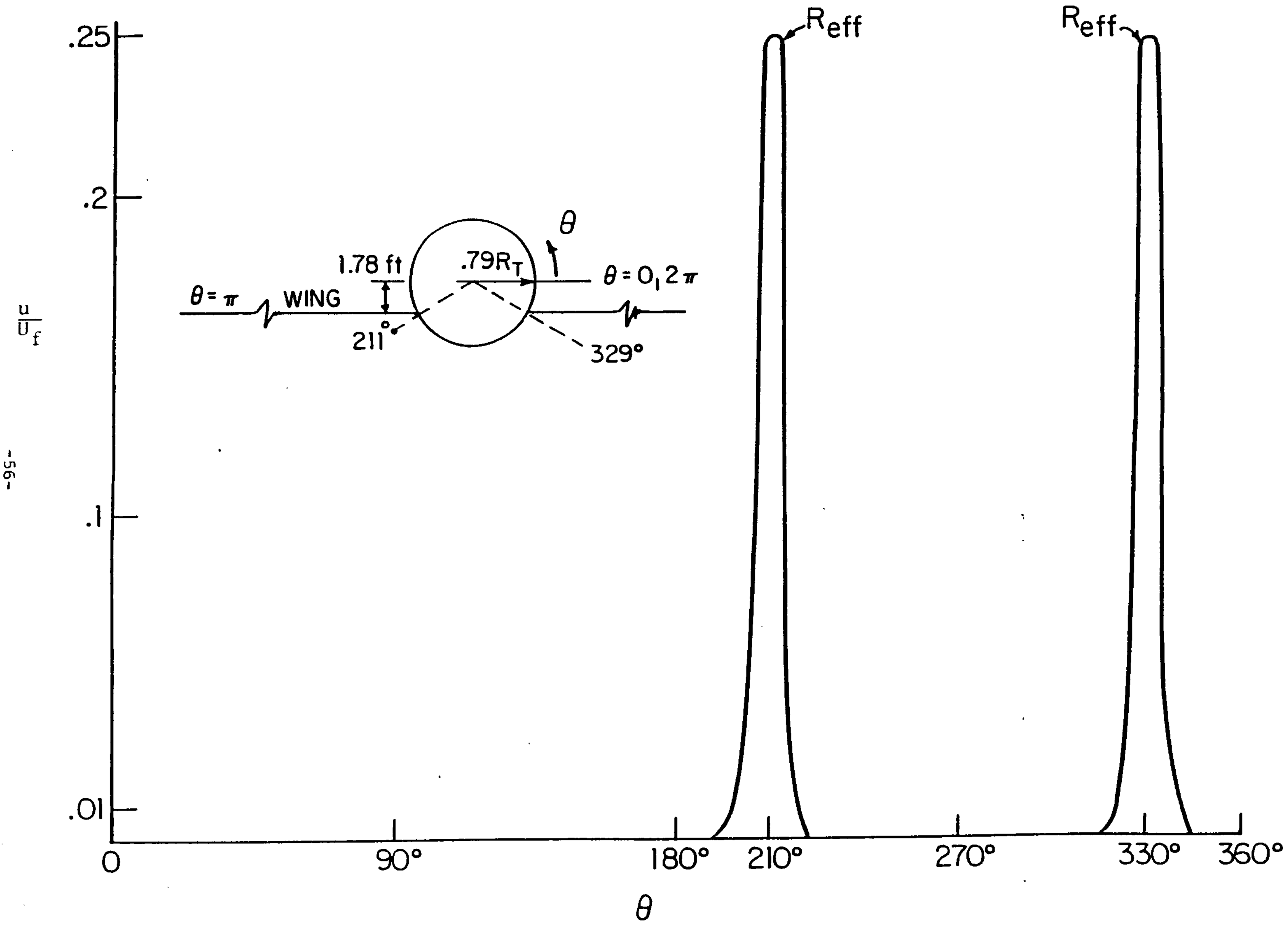

Fig. II.9 Modelled circumferential history of wing wake velocity deficit for radial station R_{eff} (based on measurements); propeller axis is at elevated nacelle position.

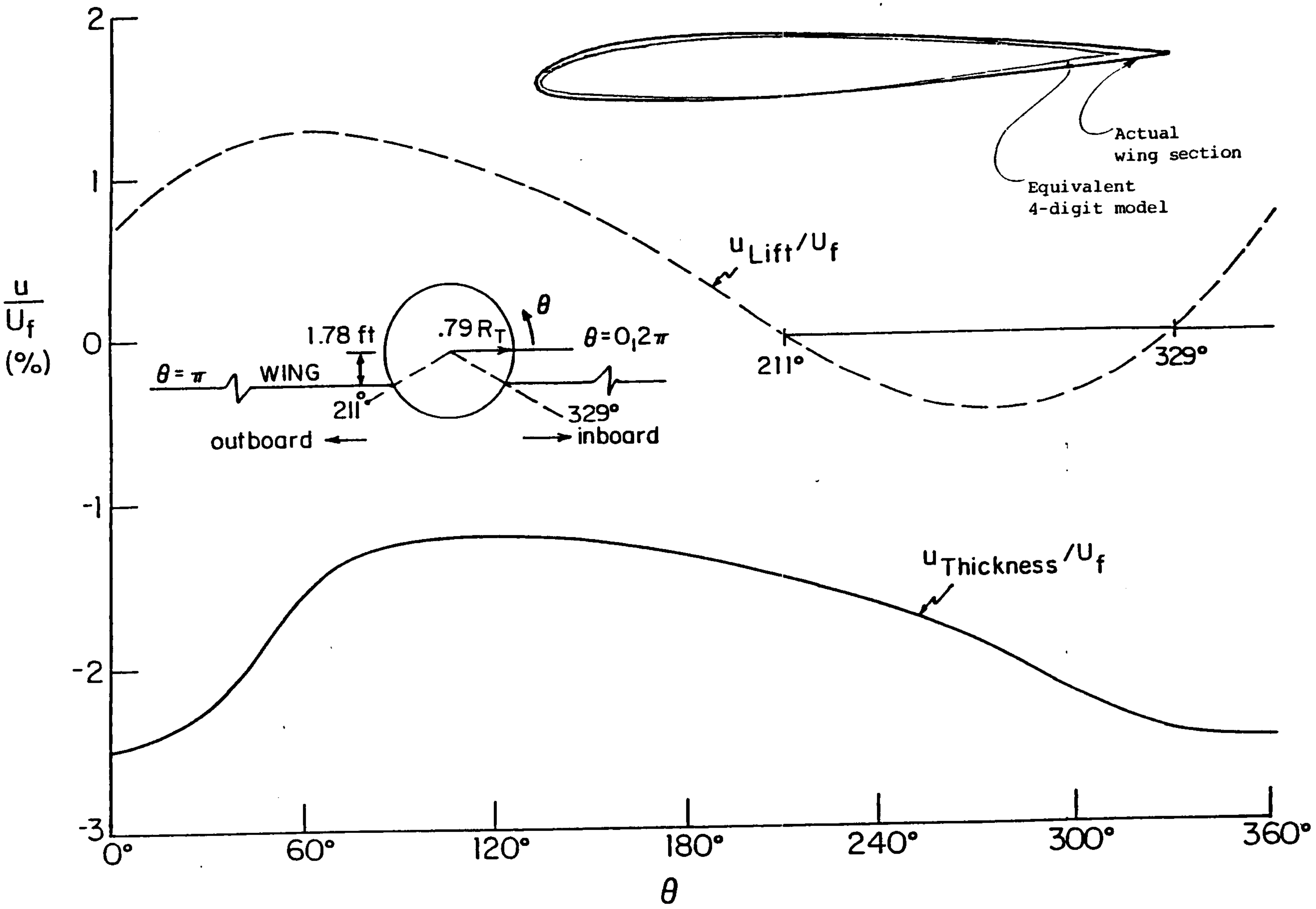

Fig. II.10 Predicted history of nonlifting and lifting wing interference flows for R_{eff} blade station.

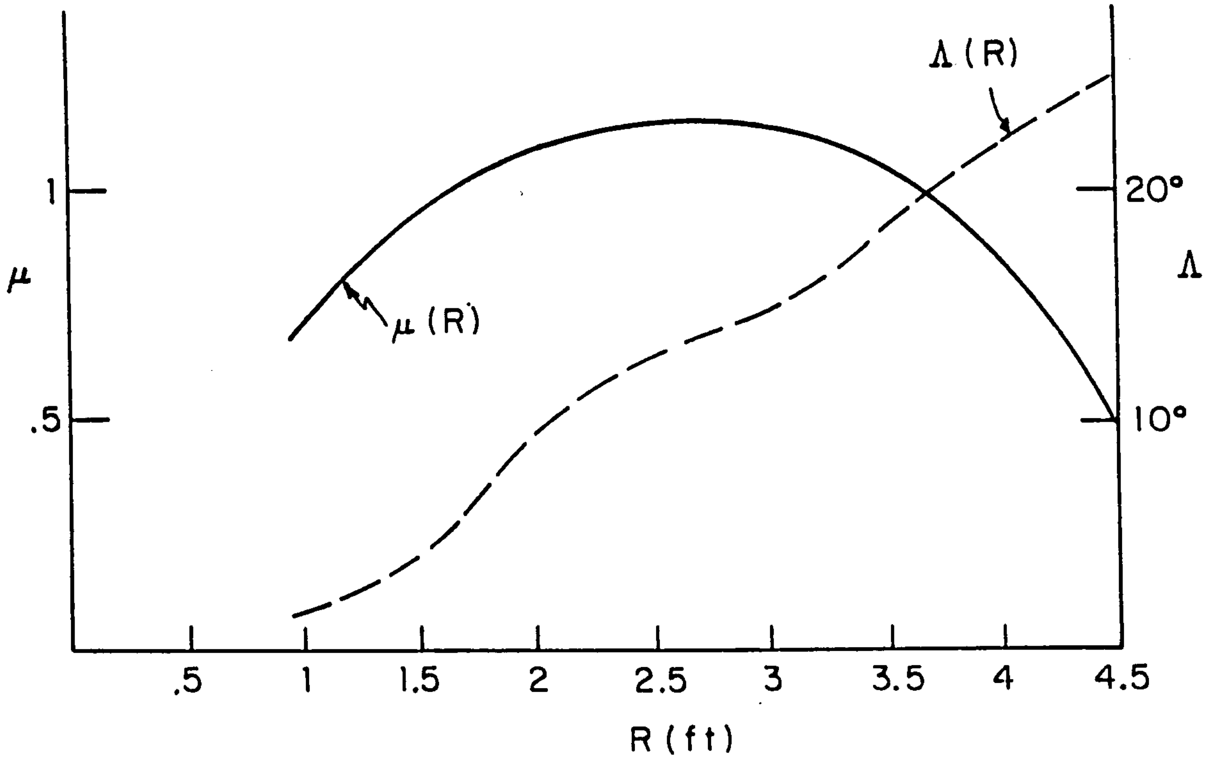

Fig. II.11 Computed values of frequency parameter μ as a function of blade radial position, and modelled component of circumferential blade sweep.

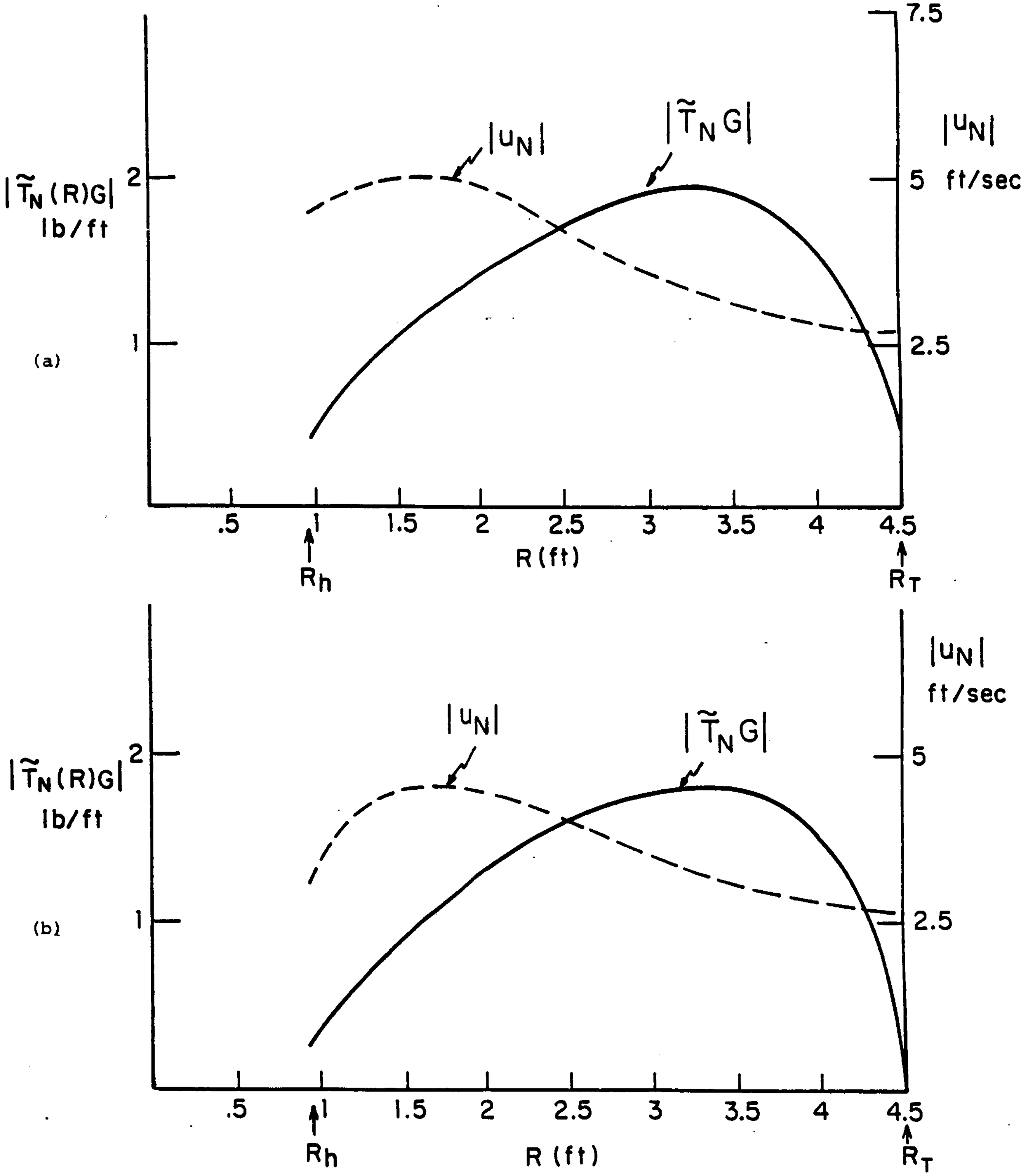

Fig. II.12 Computed fundamental of velocity deficit vs blade radial position (amplitude of gust), and calculated sectional loads for:
(a) propeller 32% of chord downstream of pylon trailing edge and,
(b) 100% chord downstream.

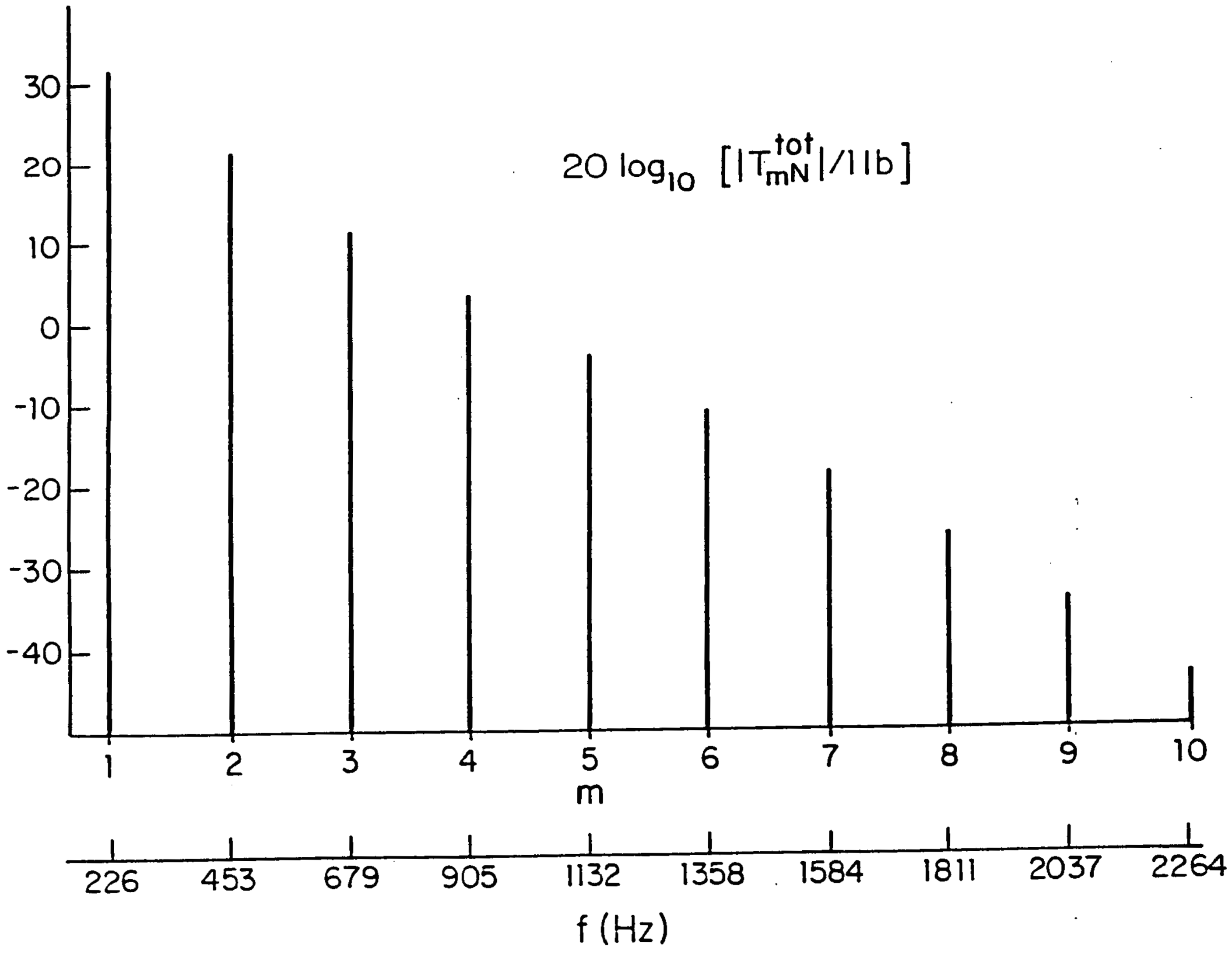

Fig. II.13 Predicted spectrum of thrust propeller force (re 1 lb), for propeller 32% of chord downstream of pylon trailing edge.

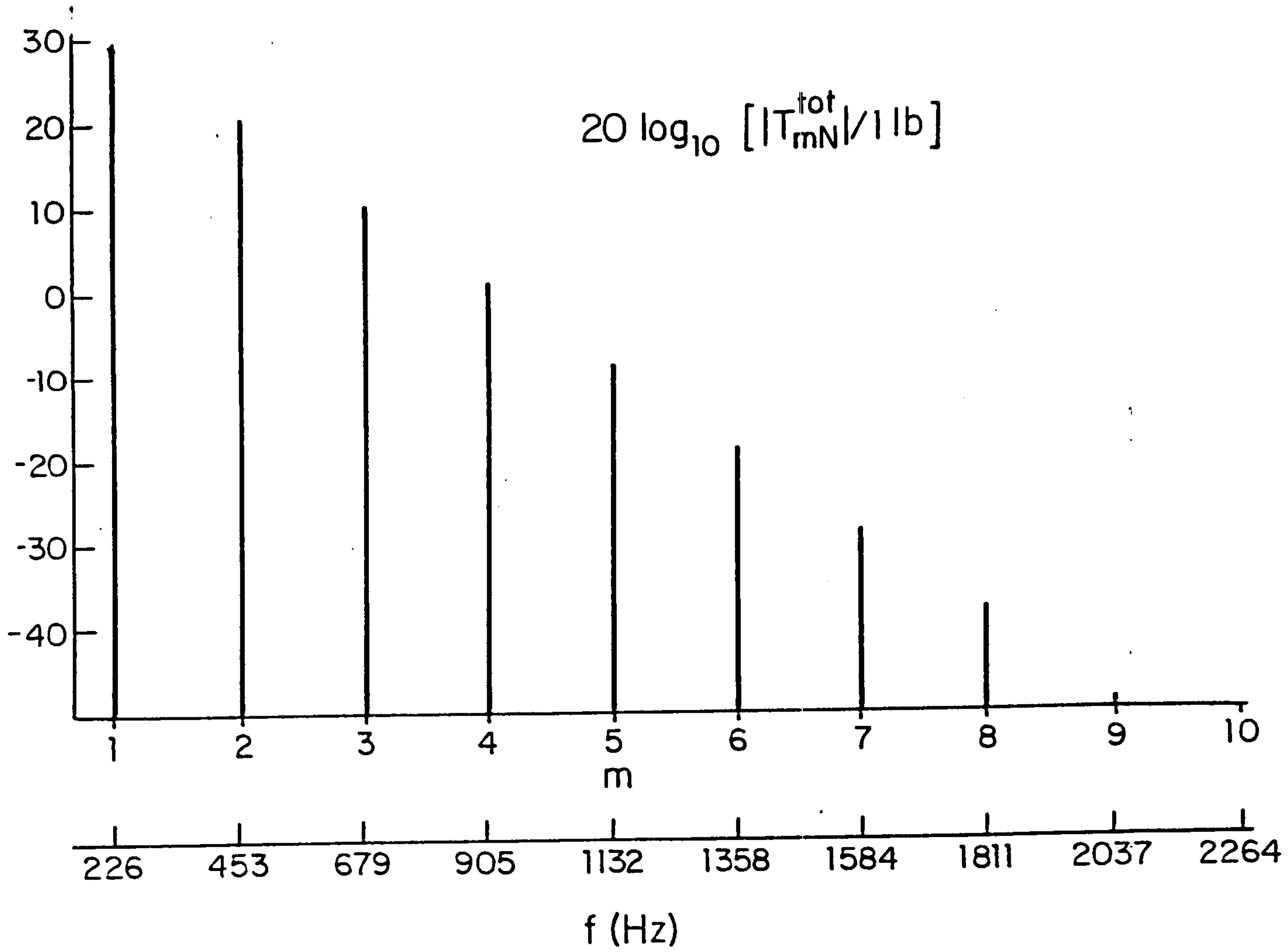

Fig. II.14 Predicted spectrum of thrust propeller force (re 1 lb), for propeller 100% of chord downstream of pylon trailing edge.

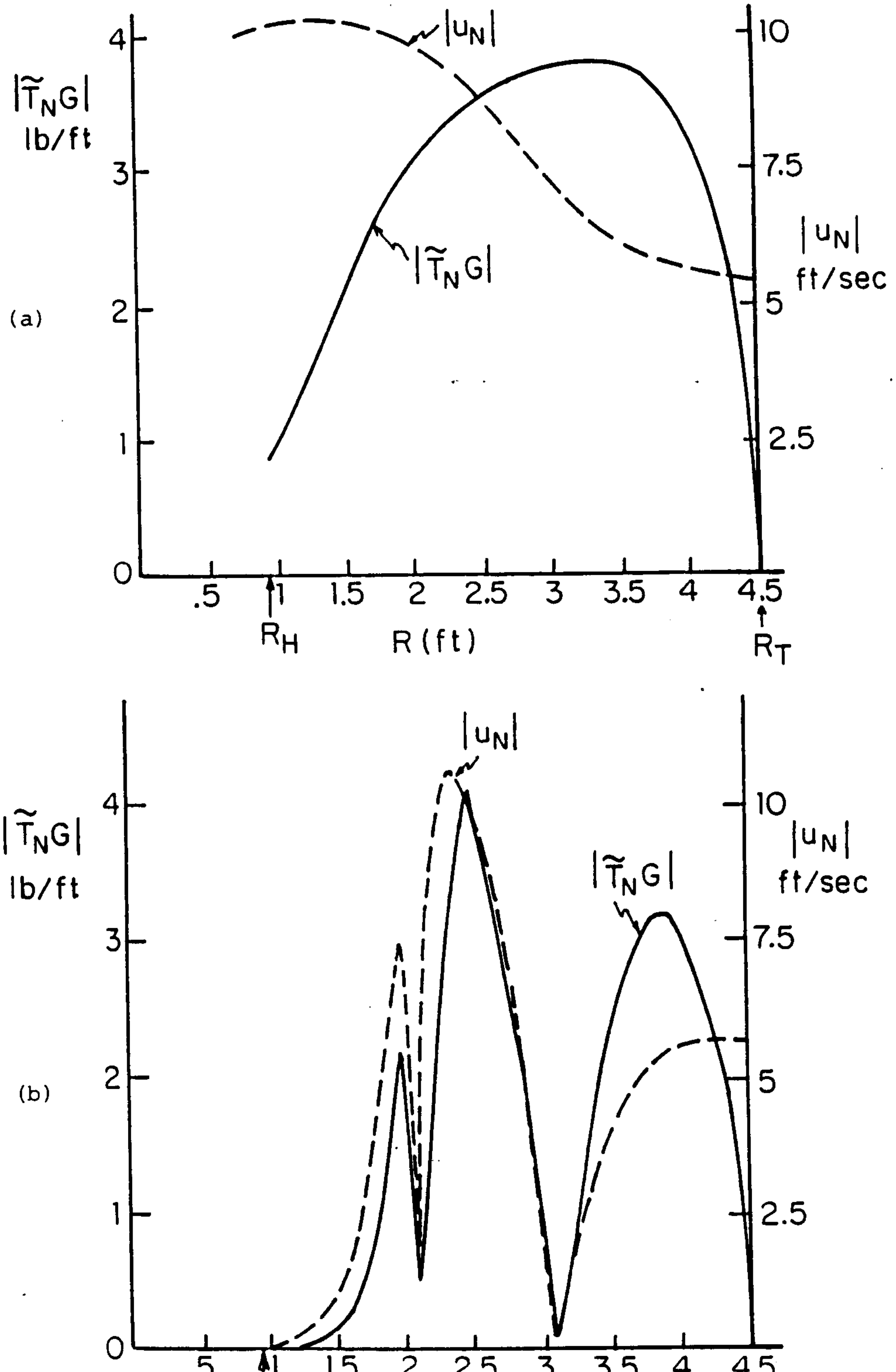

Fig. II.15 Predicted inflow fundamental and sectional load vs radial position for a wing-mounted pusher propeller; propeller position is 32%-c_w downstream of trailing edge: (a) propeller axis on wing plane, (b) propeller axis at elevated nacelle position (1.78 ft).

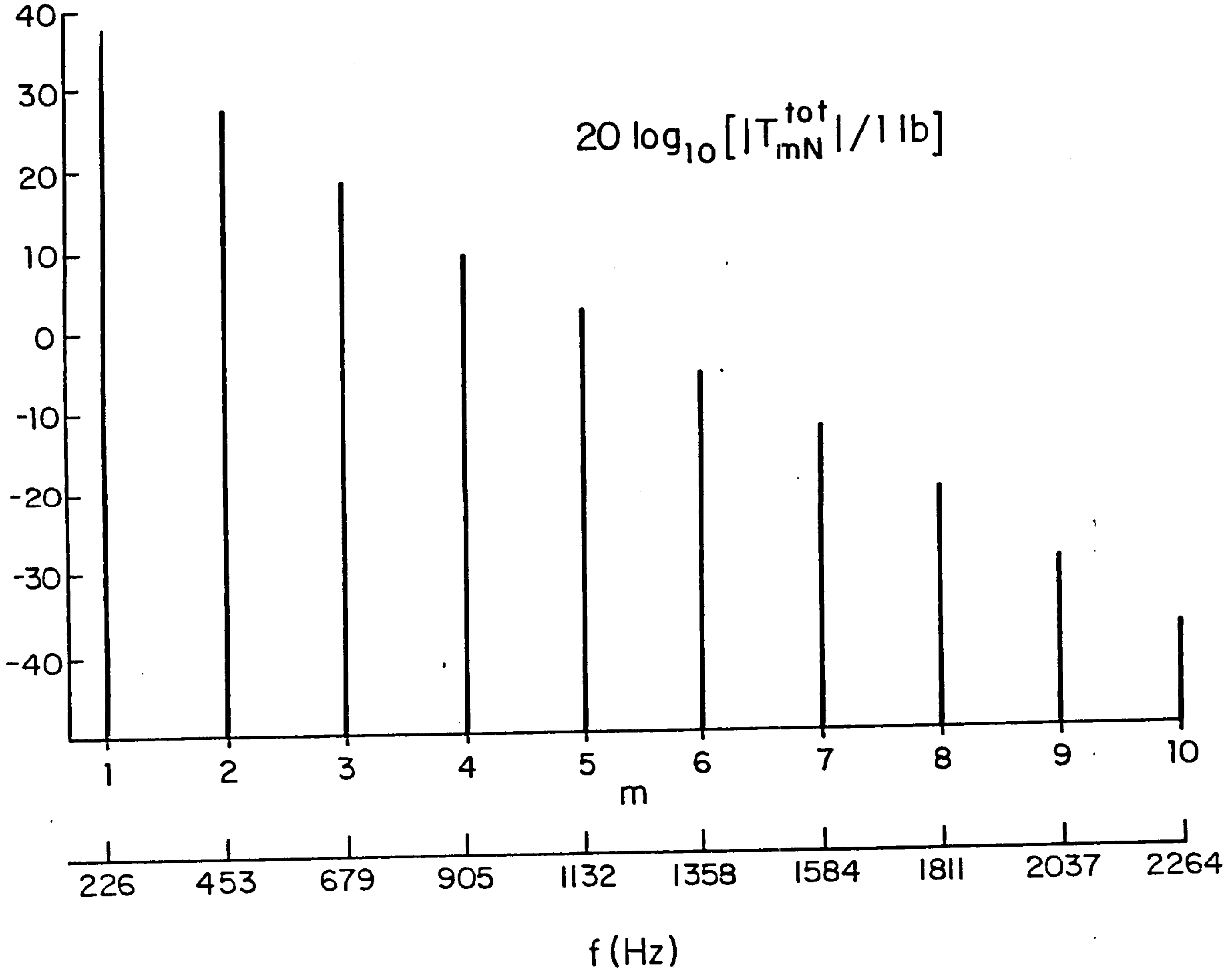

Fig. II.16 Predicted spectrum of thrust propeller force (re 1 lb), for wing-mounted pusher propeller; axis is on wing plane, propeller is 32%-c_w downstream of trailing edge.

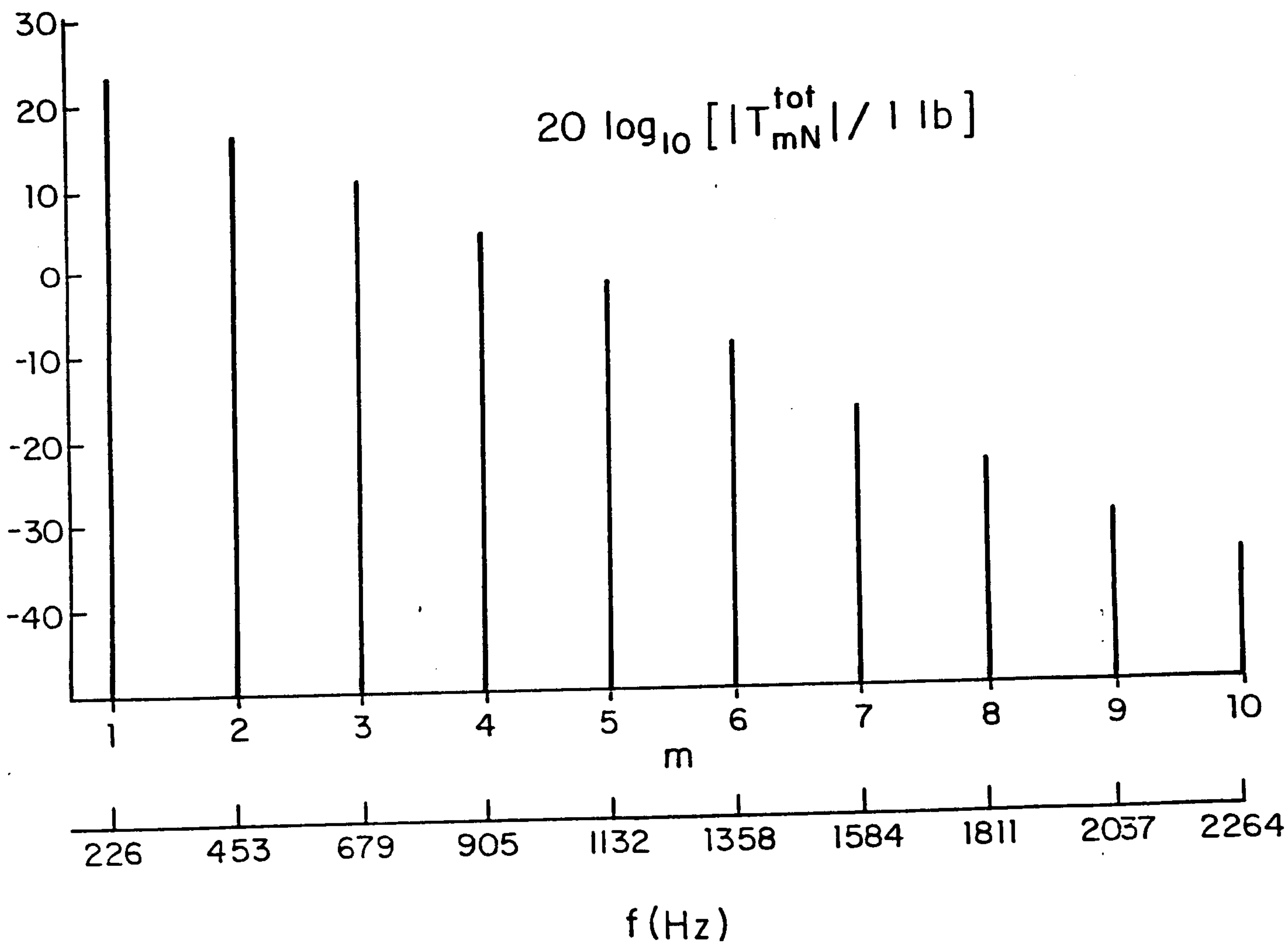

Fig. II.17 Predicted spectrum of thrust propeller force (re 1 lb) for wing-mounted pusher propeller; axis is at elevated nacelle position (z_{o_f}=1.78 ft); propeller is 32%-c_w downstream of trailing edge.

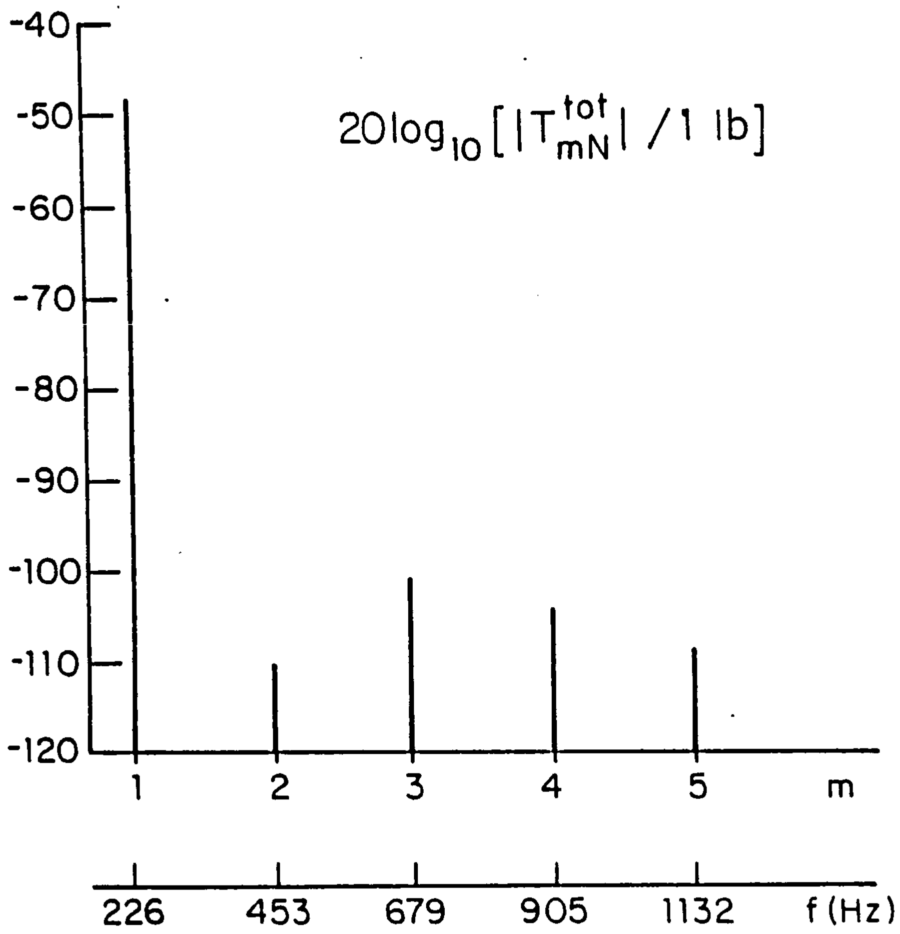

Fig. II.18 Predicted spectrum of thrust propeller force (re 1 lb) due to upstream wing interference for wing-mounted tractor propeller (cf. Figs. II.7,10); axis is at elevated nacelle position (z_{o_f}=1.78 ft).

for single vortex

$$w = \frac{\Gamma}{2\pi} \quad \frac{\tilde{y}-\tilde{y}_o}{(\tilde{y}-\tilde{y}_o)^2 + h_o^2}$$

$$y_o = R\cos\Omega t, \; h_o = R\sin\Omega t$$

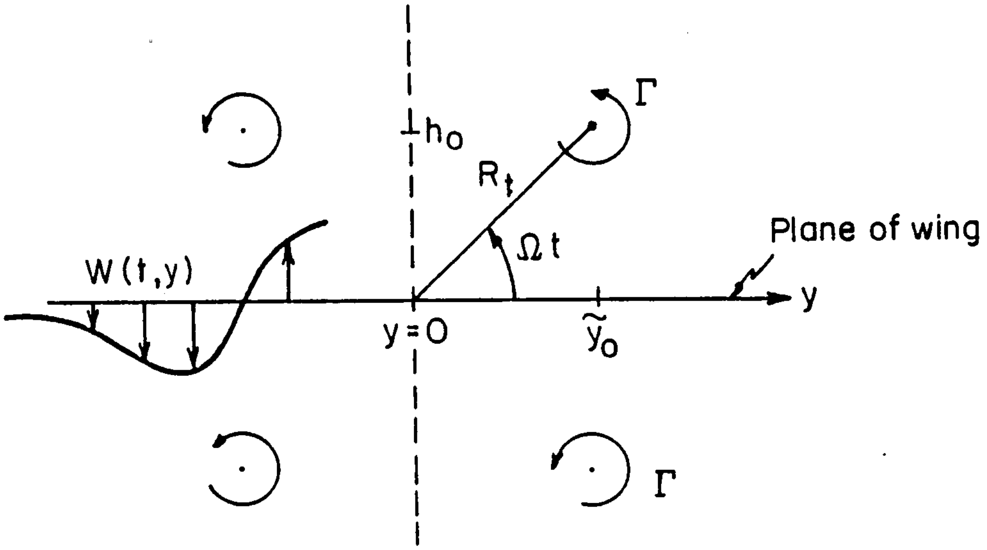

Fig. III.1 Wake model for a four-bladed propeller, indicating horizontal plane of wing and vortex-induced downwash.

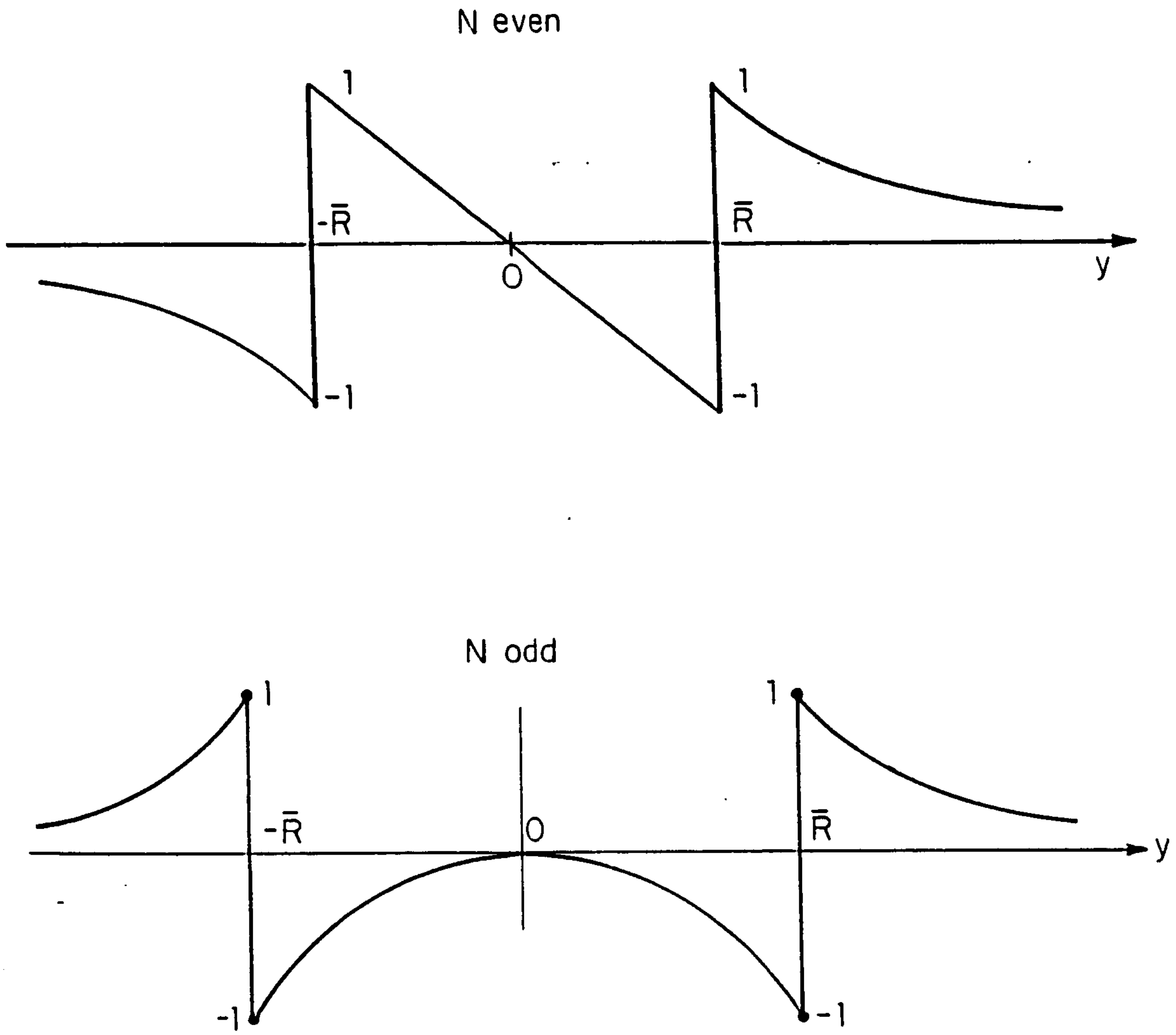

Fig. III.2 Spanwise behavior of normalized downwash fundamental $4\pi R_t w_N/\Gamma N$ for: (a) even-bladed propeller; (b) odd number of blades.

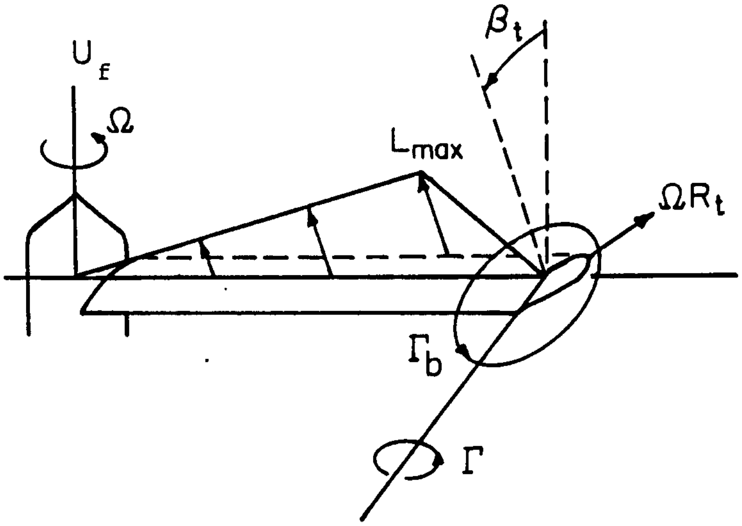

Fig. III.3 Assumed triangular distribution for steady blade lift for calculation of vortex strength.

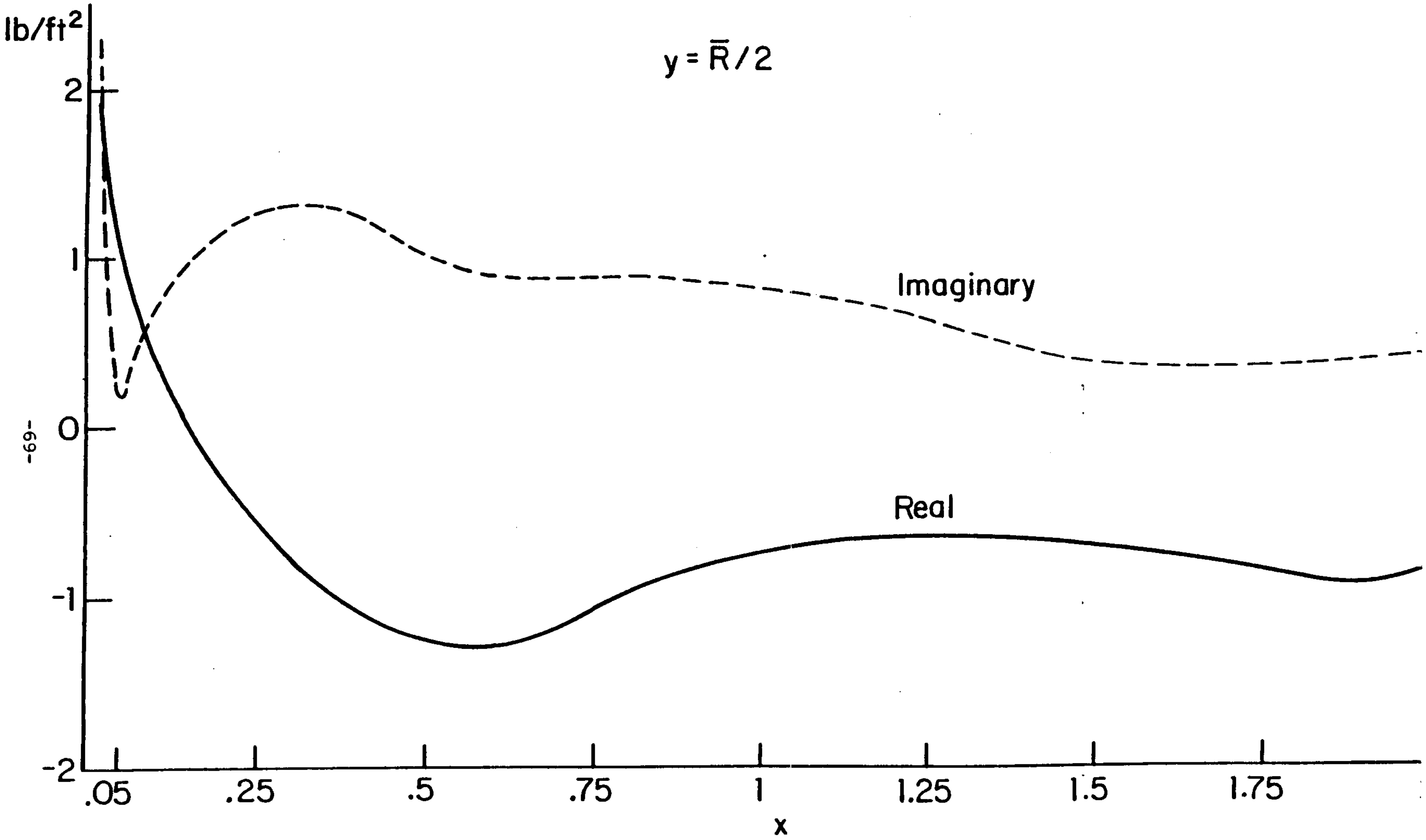

Fig. III.4 Predicted pressure distribution for wing chord at $y=\bar{R}/2$.

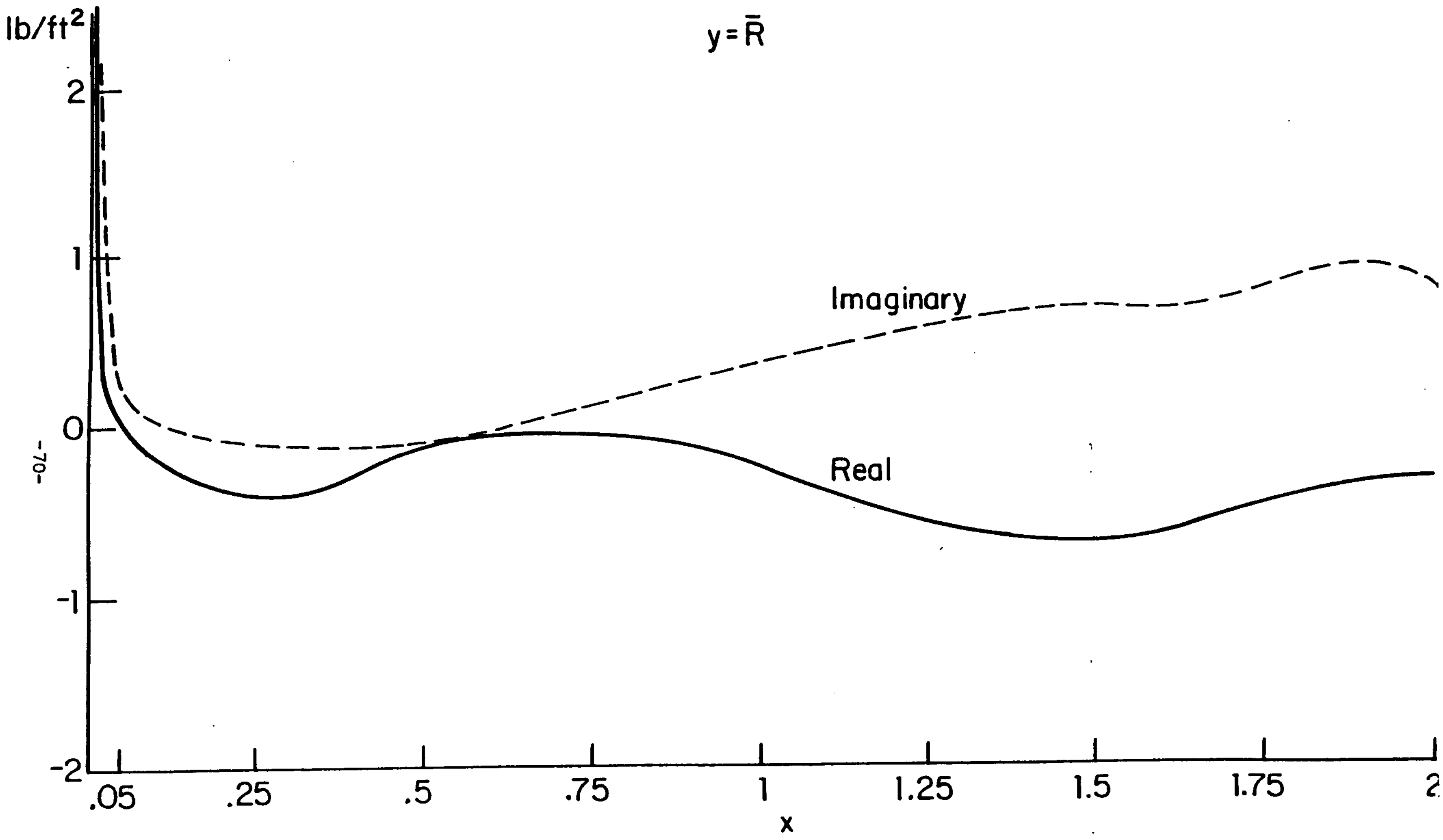

Fig. III.5 Predicted pressure distribution for wing ahord at y=R̄.

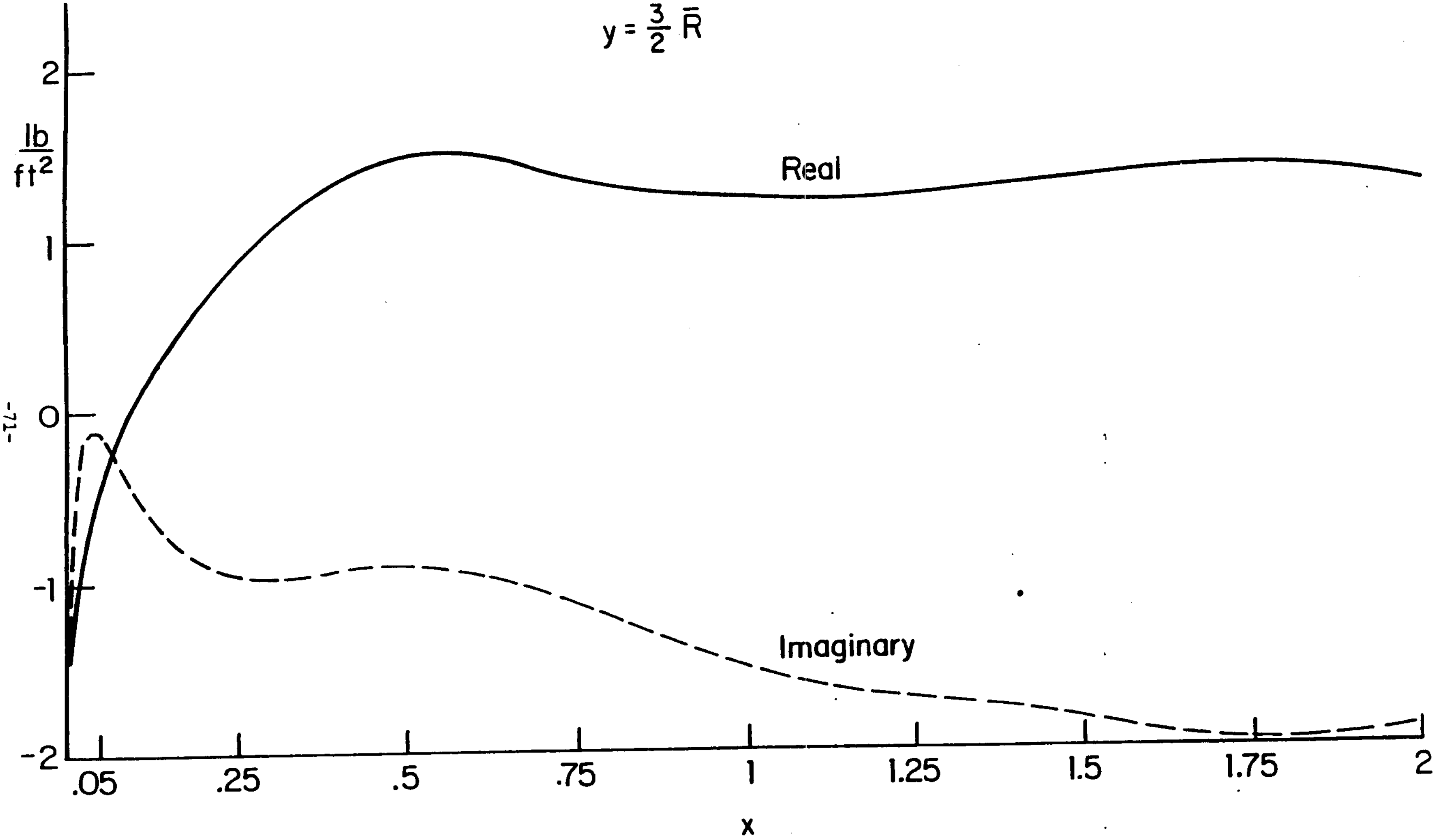

Fig. III.6 Predicted pressure distribution for wing chord at $y=\frac{3}{2}\bar{R}$.

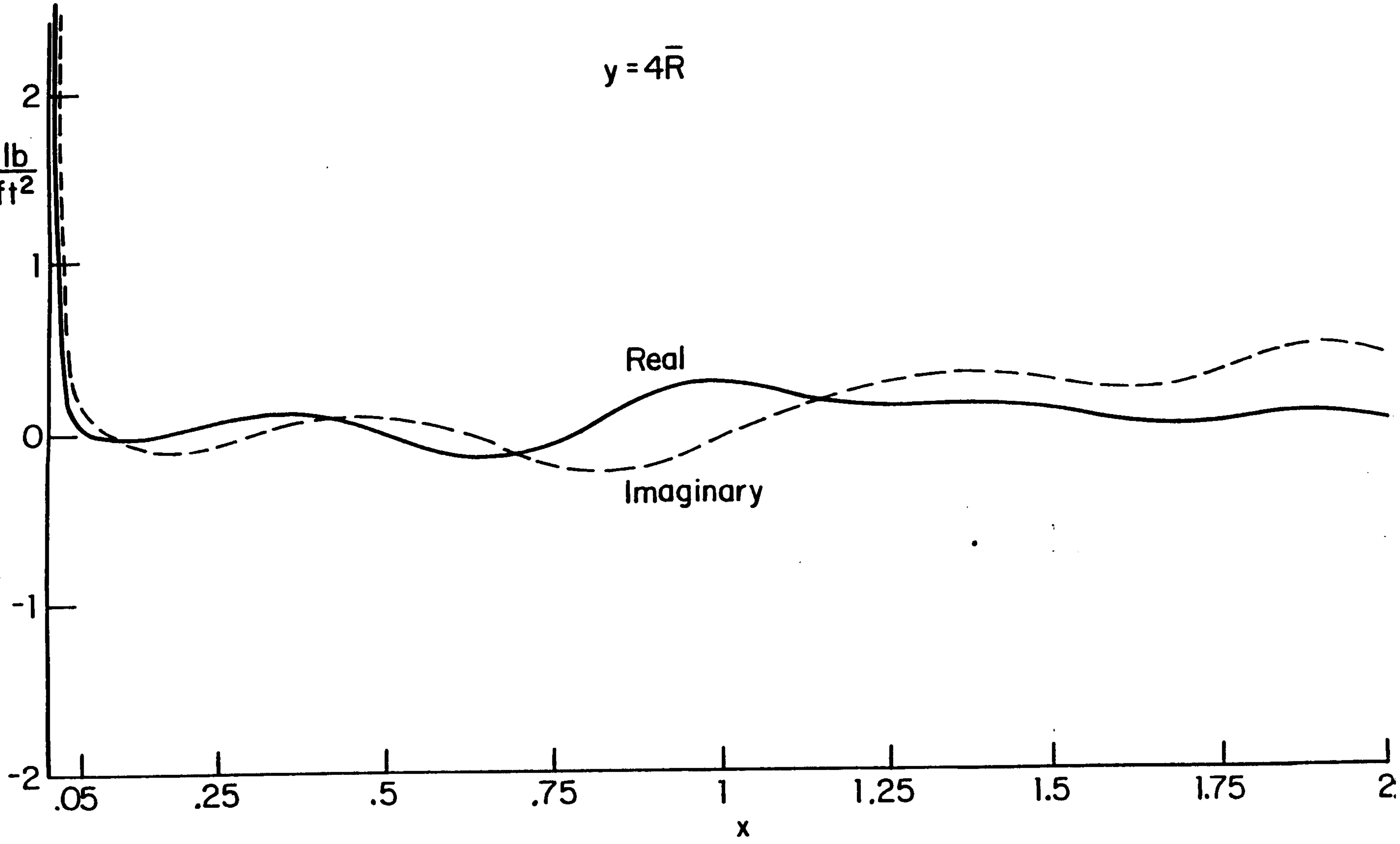

Fig. III.7 Predicted pressure distribution for wing chord at $y=4\bar{R}$.

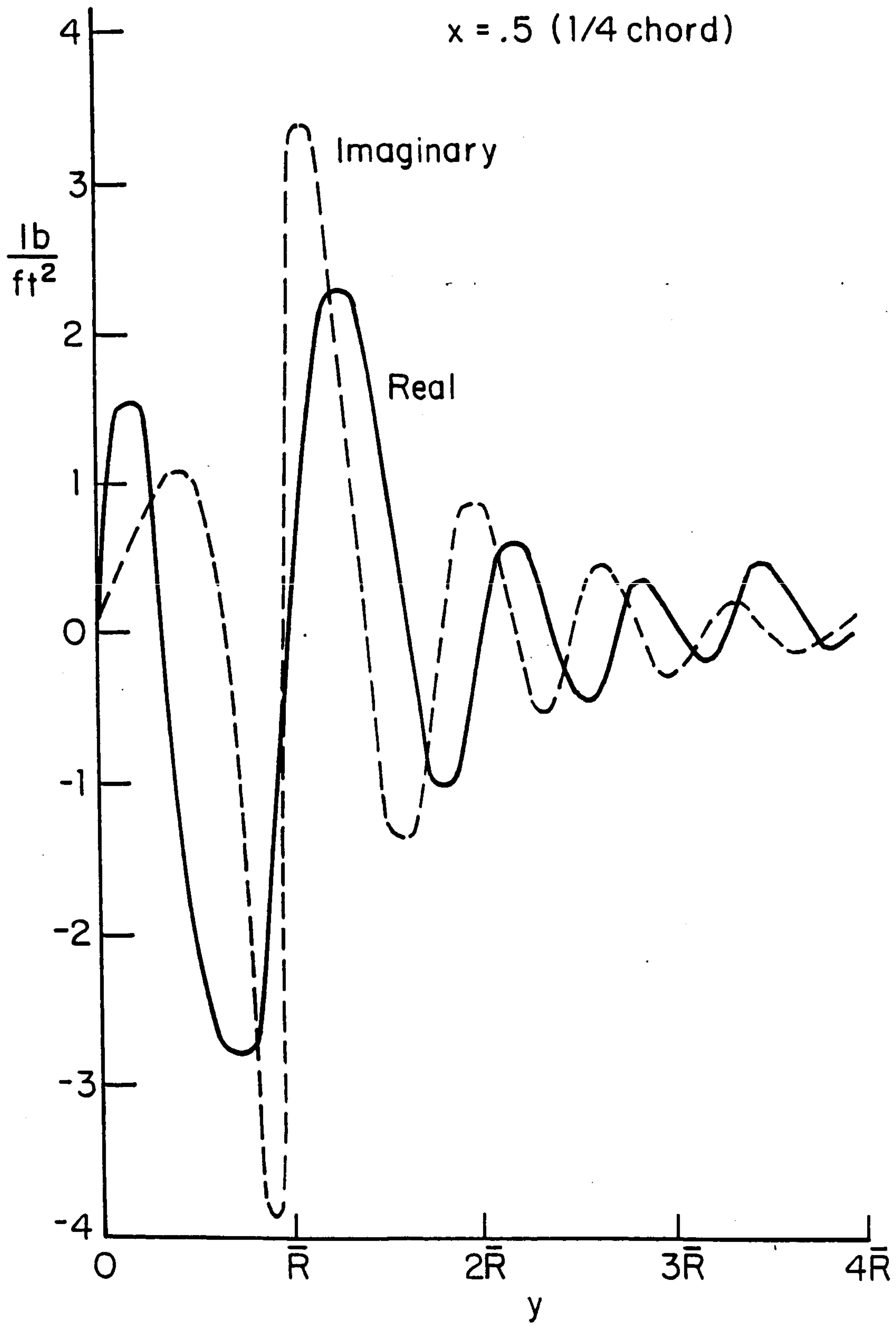

Fig. III.8 Predicted spanwise pressure distribution for chord point x=.5 (1/4 chord).

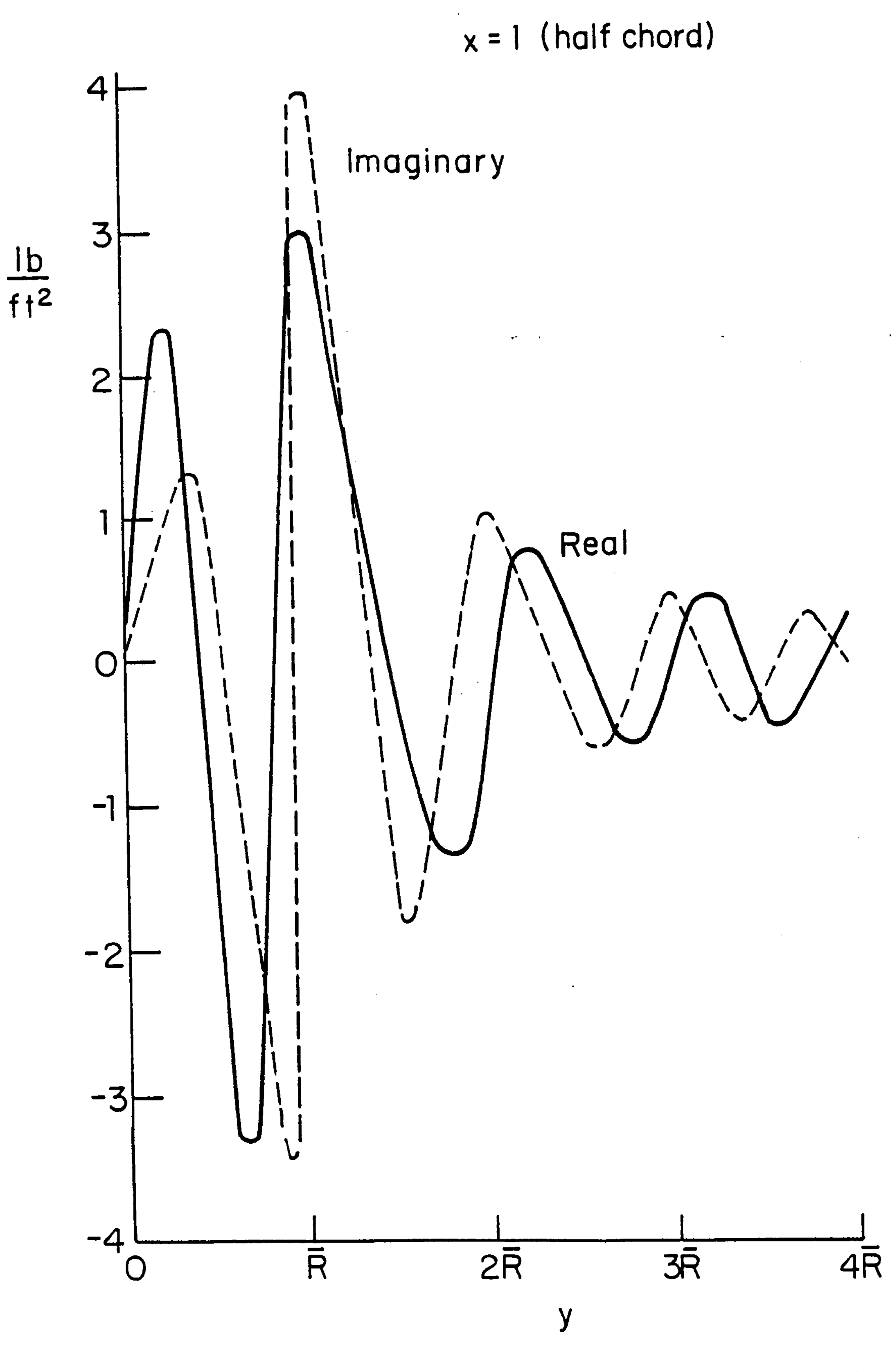

Fig. III.9 Predicted spanwise pressure distribution for chord point x=1. (1/2 chord).

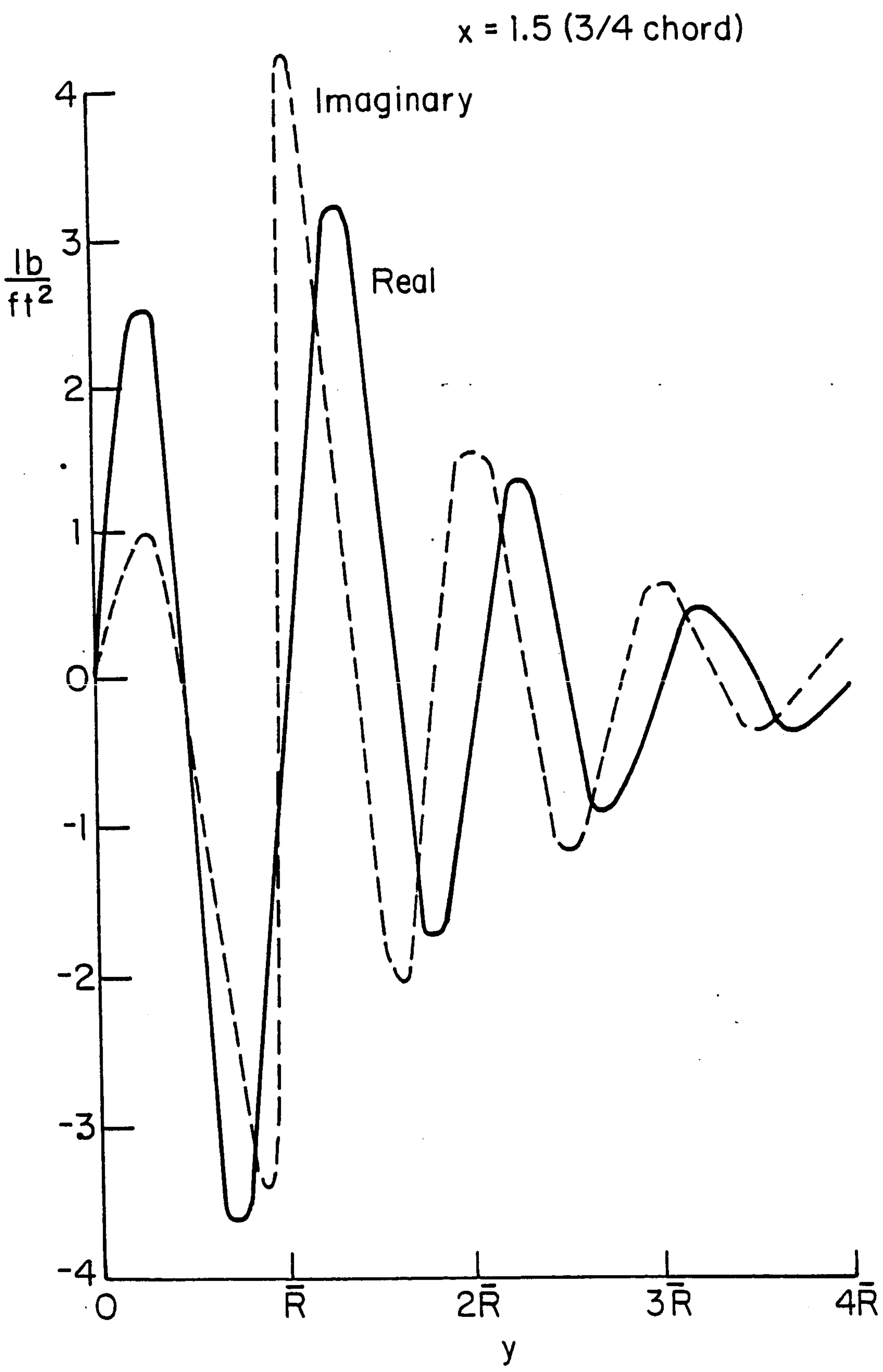

Fig. III.10 Predicted spanwise pressure distribution for chord point x=1.5 (3/4 chord).

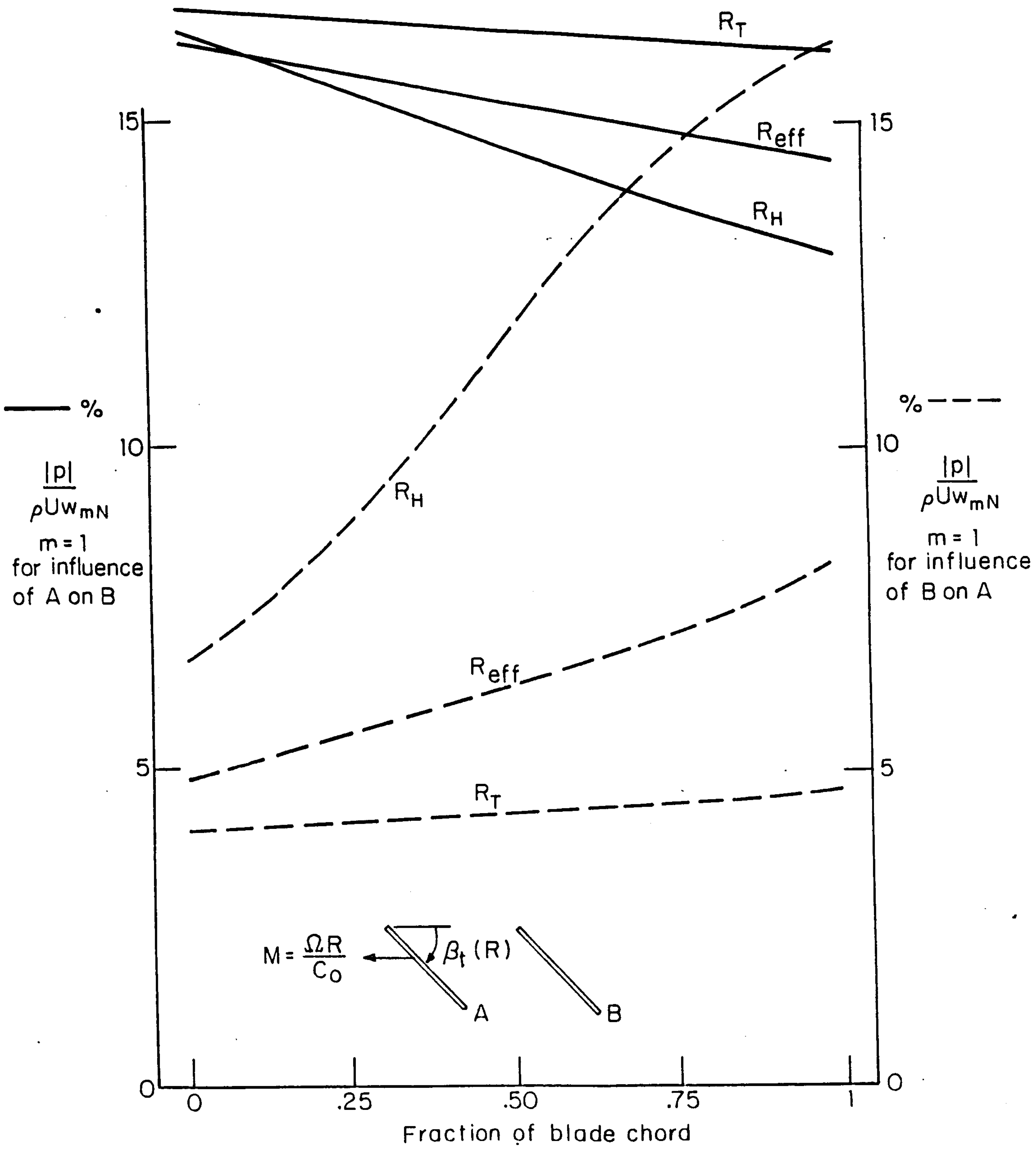

Fig. A.1 Calculated unsteady interference through direct pressure fields, dashed lines show backscatter of blade B on A, solid lines show forward scatter (blade A on B).

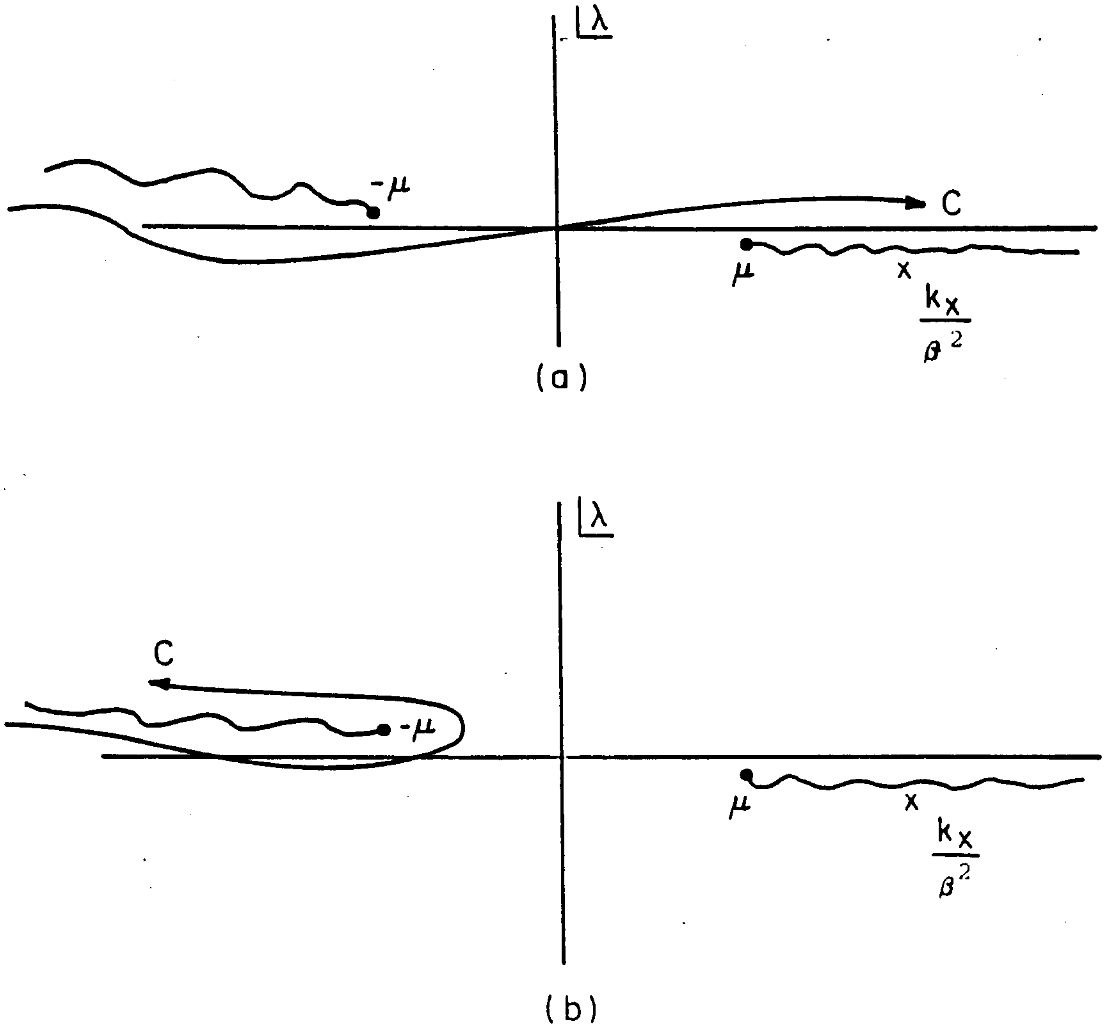

Fig. A.2 Contour integrals for calculation of induced flows.

R	β_t
R_h	76.05°
R_{eff}	57.57°
R_t	50.58°

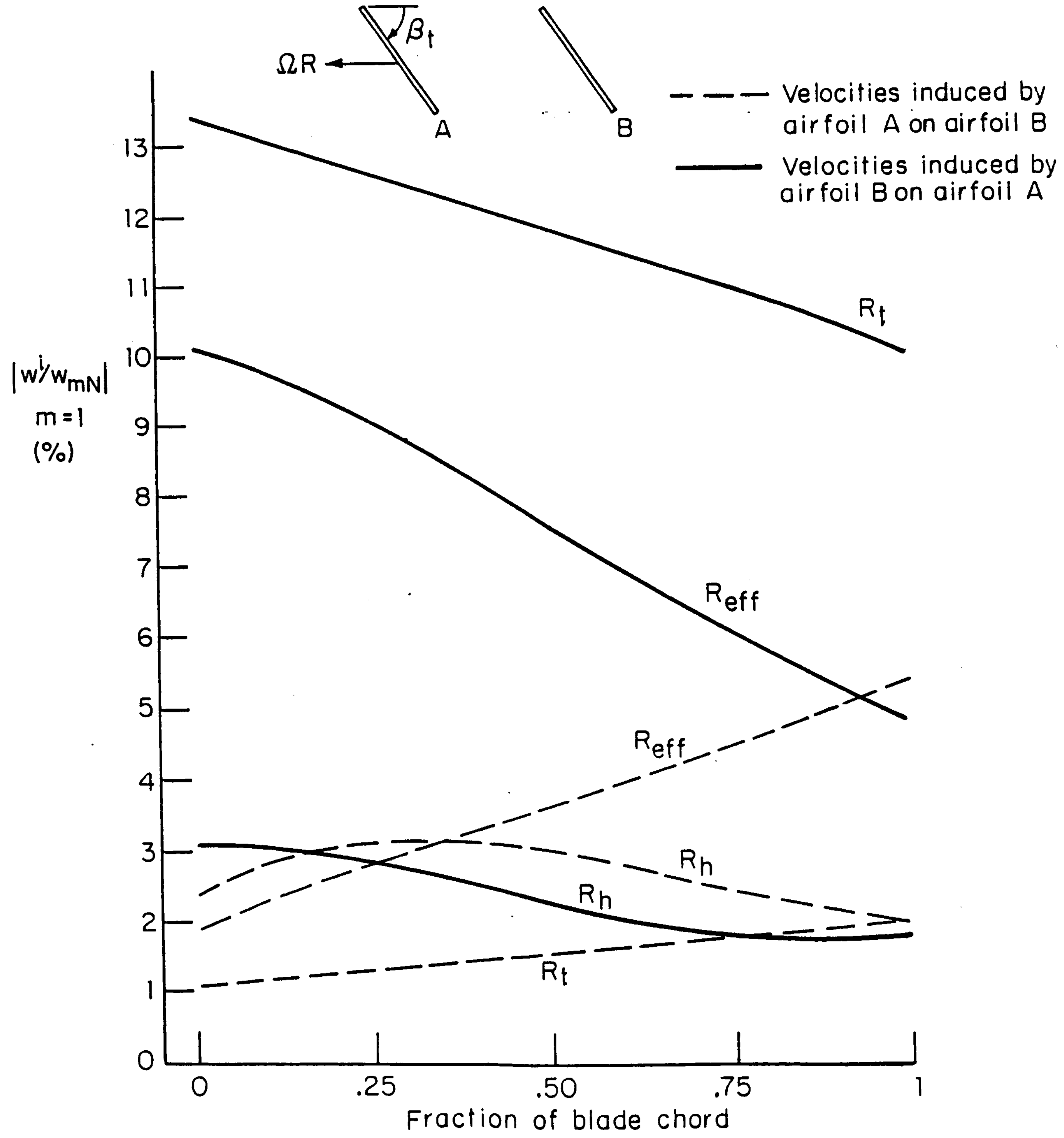

Fig. A.3 Calculated unsteady interference through induced flows; dashed lines indicate influence of airfoil B on A; solid lines that of A on B.

Standard Bibliographic Page

1. Report No.
NASA CR-178298

2. Government Accession No.

3. Recipient's Catalog No.

4. Title and Subtitle
Predictions of Wing and Pylon Forces Caused by
Propeller Installation

5. Report Date
May 1987

6. Performing Organization Code

7. Author(s)
Rudolph Martinez

8. Performing Organization Report No.
U-1411-349.10

9. Performing Organization Name and Address
Cambridge Acoustical Associates, Inc.
54 CambridgePark Drive
Cambridge, MA 02140

10. Work Unit No.
535-03-11-03

11. Contract or Grant No.
NAS1-18020

12. Sponsoring Agency Name and Address
National Aeronautics and Space Administration
Washington, DC 20546

13. Type of Report and Period Covered
Contractor Report

14. Sponsoring Agency Code

15. Supplementary Notes

Langley Technical Monitor: William H. Mayes

16. Abstract

Replacement of current turbojets by high-efficiency unducted propfans could have the unfortunate side effect of increasing cabin noise, essentially because unsteady-aerodynamic mechanisms are likely to be introduced whereby some of the energy saved may be lost again, to the production of propeller noise and to wing/pylon vibrations coupling to the cabin as a sounding board. The present study estimates theoretically associated harmonic aerodynamic forces for two candidate configurations: (1) a pusher propeller which chops through the mean wake of the pylon supporting it, and in the process generates a blade-rate force driving the structure, and (2) a tractor wing-mounted propeller, whose trailing rotating wake induces an unsteady downwash field generating unsteady wing airloads. Reported predictions of such propfan aerodynamic sources of structure-borne sound, or vibration, could be the basis for devising means for their mechanical isolation, and thus for the effective interruption of the structural noise path into the cabin. Both mechanisms are analyzed here taking advantage of the high subsonic Mach number and high reduced frequency of the interaction between the impinging flow and the affected aerodynamic element.

17. Key Words (Suggested by Authors(s))
Propfan Installation Effects
Structure-borne Noise
Unsteady Aerodynamics

18. Distribution Statement
Unclassified - Unlimited

Subject Category 71

19. Security Classif.(of this report)
Unclassified

20. Security Classif.(of this page)
Unclassified

21. No. of Pages
81

22. Price
A05

For sale by the National Technical Information Service, Springfield, Virginia 22161

NASA Langley Form 63 (June 1985)